Robotics and Computer Integrated Manufacturing 55 (2019) 109–128

Contents lists available at ScienceDirect

Robotics and Computer Integrated Manufacturing

journal homepage: www.elsevier.com/locate/rcim

A modular mobile robotic architecture for defects detection and repair in narrow tunnels of CFRP aeronautic components

Simone Pio Negri[a], Vito Basile[a,*], Marcello Valori[a], Benedetto Gambino[b], Irene Fassi[c], Lorenzo Molinari Tosatti[c]

[a] Institute of Industrial Technologies and Automation, National Research Council of Italy, Via P. Lembo 38F, Bari I-70124, Italy
[b] Leonardo Aircraft, Structural Analysis and Methods, Zona ASI – Località Incoronata, Foggia I-71100, Italy
[c] Institute of Industrial Technologies and Automation, National Research Council of Italy, Via A. Corti 12, Milano I-20133, Italy

ARTICLE INFO

Keywords:
Mobile robotics
Manufacturing
Composite
Repair
CFRP

ABSTRACT

Advanced composite structural components in aeronautics are characterized by very high production costs because of their dimensions, complex shapes and expensive forming equipment. For these components, such as horizontal stabilizers and wings, a defect occurrence is often critical because large part of inner surfaces, made of long and tapered narrow tunnels, are not reachable for repair operations. In these cases, the part is rejected with a relevant economic loss and high production costs. For this reason, aircraft constructors plan huge investments for defects avoidance during the forming processes of CFRP and to develop effective, robust and reliable repair tools and methods. Mobile robotics can play an important role, with specific systems capable of moving into narrow channels of wings structures (i.e. multi spar boxes) and repair it in accordance to technical standards. This paper describes an innovative mobile robot architecture for bonded repair scarfing operations on CFRP components. Targeting and responding to the demanding machining requirements, the functional-oriented design approach clearly highlights the advantages of a modular robotic solution. The mobile robotic architecture can be also applied in other fields with similar challenging manufacturing operations for further inspection, detection and machining operations.

1. Introduction

Working in narrow space is a typical issue for the repair process of aeronautical structural components. Carbon Fiber Reinforced Plastic (CFRP) components, as wings and horizontal stabilizers, are often realized in the form of multi spar boxes assemblies. A typical example is the Boeing 787 Dreamliner horizontal stabilizer (tailplane) which has a multi-spar boxes structure and its cross-section is composed by a plurality of longitudinal tapered narrow tunnels. During the manufacturing process of these components some defects may occur. In order to reduce the high cost of discards, the necessity for an efficient and robust repair process arises. In literature, different technological processes and techniques for CFRP aircraft structures repair are available [1]. This paper deals with the application of such techniques in narrow spaces, as the multi spar boxes structures.

Currently, the CFRP repair techniques are typically performed manually [2] and sometimes the damage is not accessible by the operator. In large CFRP multi-spar boxes structural components, indeed, human operators are able to repair internal damages only if localized in proximity of the wing tip or root. In all the other cases there are no fix strategies currently available and the components, often very expensive, must be discarded [3]. Thus, the position of the damage is crucial, as it causes a large number of discards in aeronautics manufacturing, with consequent increase of the production costs.

Due to the lack of solutions of applying fixing techniques in narrow multi spar boxes, in this paper a strategy for the automation of such a process is described. Mobile robotics is identified as the key enabling technology that makes it possible. As a further advantage, some studies, remarked the importance of automated machining of CFRP and the advantages in terms of accuracy, quality and reliability compared with a manual operation [4]. Nevertheless, there are no available solutions for the repair of internal defects. The proposed approaches, indeed, consider either new specific devices to be manually fixed in proximity of the damage [5,6], or the use of conventional robots, too big for this purpose [7]. In [8] a robotic inspection cell is presented, composed of three industrial manipulators performing both, photogrammetry acquisitions and ultrasound-based NDT inspection. The robots can move along linear guides and the inspection of large components is enabled;

* Corresponding author.
E-mail address: vito.basile@itia.cnr.it (V. Basile).

https://doi.org/10.1016/j.rcim.2018.07.011
Received 26 April 2017; Received in revised form 10 May 2018; Accepted 12 July 2018

Table 1
Main features of the listed robotic architectures for operations in narrow spaces.

Robot	Application	Modular (Y/N)	Functionality	Duct section [mm]	Tethered (Y/N)	Locomotion System	Autonomy level
GE Inspection Robotics [9]	Oil, Gas, Power Plant	Y	Inspection & Cleaning	Ø 400	Y	Magnetic Wheels	Manned
Pipeline Explorer [10]	Gas Pipeline	Y	Inspection	Not specified	N	Retractable Wheels	Manned
Robotic Pipeline Inspection [13]	Water & Wastewater	Y	Inspection	Ø 305	Y	Crawlers	Manned
Solo Robot [15]	Wastewater	N	Inspection	Ø 200 ÷ 300	N	Crawlers	Self-Operating
Rover X SAT [15]	Wastewater	N	Inspection	≥ Ø 100	Y	Wheels	Manned
Versatrax [16]	Wastewater	Y	Inspection	≥ 370 × 480	Y	(Retractable) Crawlers	Manned
Piping Insp. Camera [17]	Wastewater	N	Inspection	Ø ≥ 150	Y	Wheels	Manned
ANATroller ARI 100 [18]	HVAC	Y	Inspection & Cleaning	215 × 127	Y	Wheels or Crawlers	Manned
JettyRobot [19]	HVAC	N	Inspection, Cleaning, Repair	Ø ≥ 360	Y	Retractable Crawlers	Manned
Rail Runner X (RRX) [20]	Shipbuilding Industry	N	Welding	≥ 600 × 800	Y	Crawlers	Semi-Autonomous
Fraunhofer Prototype [21]	Aeronautics	N	Wing Assembly	Not specified	N	Anthropomorphic Robot + Snake Arm	Not specified
Scarfing Robot by CNR-ITIA	Aeronautics	Y	Wing Inspection & Repair	≥ 150 × 150	Y	Omni-Directional Wheels + Pushing Rods	Semi-Autonomous

however, there is no possibility for internal defects detection.

An extended survey of the state-of-art of mobile robots for applications in confined spaces is hereafter reported. Table 1 reports a detailed summary, as well as the main features of the architecture presented in this work. The following fields are considered: power plants inspection, piping maintenance (oil & gas, water and wastewater) and HVAC (Heat, Ventilation and Air – Conditioning) applications.

The power plant maintenance field is led by General Electric Inspection Robotics [9]. This manufacturer builds small mobile robots to perform preventive services of power plants selected components, such as electric generators, turbines, boilers, tanks and piping. These robots are based on modular components, which can be standard, modified, or even customized upon request. The main operations are remote visual inspection (RVI), not destructive inspections (NDI – as ultrasonic inspection or eddy current) or even cleaning, polishing, grinding and painting. However, this kind of robot is too big to navigate inside the narrow tunnels featured by aeronautical components. Moreover, they lay on magnetic wheels that are not suitable with CFRP products.

The second application concerns piping inspection, required by several fields, as chemical plants, oil & gas pipelines, water and wastewater treatments and transportation. The “Pipeline Explorer” mobile robot by the “National Robotics Engineering Center - Carnegie Mellon University” [10] is the first untethered, remotely-controlled robot for inspecting live underground natural gas distribution pipelines. This robot represents the state of the art in remote-controlled inspection systems for low-pressure and high-pressure natural gas pipelines. The battery-powered Explorer robot can perform long-range, extended duration visual inspections of cast-iron and steel gas mains. As innovative feature, the pitch-roll joints are highlighted, used in place of pitch-only joints. These specific-designed joints allow orientation of the robot within the pipe, in any direction needed. Furthermore, three radial retractile legs are linked to custom-molded driving wheels, aimed to the correct positioning in the tube cross-sectional planes [11,12].

PureRobotics™ commercializes the “Robotic Pipeline Inspection” [13] to inspect pipes down to diameters of 30.5 cm (12″). The PureRobotics pipeline inspection system performs multi-sensor surveys in dry pipe or while submerged, with an operation range of up to 3 kms away from the access point. The subsystems are remotely-operated tracked vehicles tethered by a fiber optic cable.

However, the above described devices do not fit the narrow spaces typical of aeronautical components, due to their sizes. The “Solo Robot”, by RedZone Robotics [14], represents a solution conceptually similar, but complying with the typical inner dimensions of aeronautical structures, but it is not sufficiently stiff to allow light machining and cleaning operations.

Other relevant examples (with similar limitations), are the robot “Rover X SAT” by Envirosight [15], the robot “Versatrax” by Inuktun [16] and the “Piping Inspection Camera” by Schroder [17]. In particular, the “Versatrax” robot implements a locomotion system that mixes up the concept of crawlers and that of arms pushing upon pipe walls.

In the field of HVAC service robots, a wide range of solutions exists, due to the high diffusion of HVAC systems in the last decade. A relevant feature is the transversal rectangular section of several HVAC piping systems, more comparable to the inner shape of aeronautical components than the circular one.

The ANATRoller robot family, by Robotic Design [18], consists of mobile tethered robots, developed in various sizes, able to move inside HVAC ducts, capable to overcome relevant slopes and perform specific tasks (i.e. spraying solvents for cleaning purpose) in a wide range tunnel shapes. However, this kind of architecture is not suitable for performing machining operation due to the underweight of the subsystems.

A very particular application in HVAC mobile robot service is the JettyRobot by Neovision [19], extending some concepts of the already described “Versatrax” robot. Its specific mechanical architecture, characterized by six multi arms equipped by six crawler units, is suitable for all circular ducts: horizontal, vertical, ascent and descent, and

a special extension is available also for rectangular ducts. However, working in ducts with diameters down to 360 mm, it does not comply with typical aeronautical structure sizes. In shipbuilding industry, welding is a fundamental process which can be critical for several reasons such as: 1) dangerous for operators since it is performed in hazardous environment; 2) it is executed in the double-hulled structure of the ship. For this specific application other authors proposed the "Rail Runner X" robot which is described in [20] where a 7 DoF robot is concepted and designed for semi-autonomous welding operations. A concept solution of industrial robot acting inside narrow spaces in aeronautical components, developed by the Fraunhofer Institute for Machine Tools and Forming Technology, is described in [21]: a mobile robot is equipped with an articulated arm, consisting of eight series-connected links, capable to rotate with extremely wide ranges of motion, in order to reach the furthest extremities of the wingbox cavities. The arm is a "snake arm robot", with a maximum payload of 15 kgs and a maximum reach of 2.5 m. However, this latter feature is not compliant with the length of most wings and stabilizers in aeronautics industry. Another similar implementation of this solution is presented in [22].

A general purpose robot (SHeRo) for maintenance and repair operations is described in [23]. It is an example of hexapod robot particularly suitable for unstructured and hazardous environments. Its scalability enables the applicability to restricted spaces, however this concept is not tailored for narrow tunnels and aircraft manufacturing since its architecture is cumbersome and not enough stiff for scarfing/cutting operations.

As result of the survey, the following considerations apply: working in narrow spaces implies a strongly application-oriented mechanical design for the robotic solution and a customized electronic apparatus for the multi-sensor inspection system. Taking into account the production costs of the aeronautical components, in this paper it is pointed out the necessity of advanced repairing systems and a new modular mobile robotic system is proposed. Starting from an accurate analysis of the repairing process (Section 2), manufacturing and robotic requirements are identified (Section 3), and a customized novel solution is proposed, detailing its architecture (Section 4), kinematics (Section 5) and control strategy (Section 6); in Section 7 the working functionalities are simulated and discussed.

2. Defect detection and repair process on CFRP structures

In this section, the most diffused repair technique for CFRP structural components is described, with particular reference to multi-spar boxes structures. It is analyzed as a general purpose technique, but contextualized for the manufacturing process of large structural components with narrow tunnels inside. The same technology can be efficiently applied to components damaged during service, due to impact damages (dropped tools, bird strike, service collisions, etc.) or environmental exposure (moisture ingression, lightning strike, rain erosion, hail, UV radiation, etc.). In this latter case, the repair is more complex because the part must be disassembled, causing the aircraft to be temporarily out of service.

With regards to the repair technology, bonded composite scarf repairs are widely used, because they ensure high efficiency of joints [24,25], adequate reliability [26–28] and high finishing of sculptured surfaces [3,33]. This latter aspect is very important for the repair of external aerodynamic surfaces (external skin panels). Furthermore, several research studies proved that this repair technology ensure higher performance and reliability than other repair techniques (resin injection and doubler-based techniques, mechanically fastened patches, etc.). For these reasons, bonded composite scarf repairs are increasingly applied in aeronautics manufacturing with successful results, and a relevant research effort is currently focused on this technology in order to improve its efficiency and solve the open issues [1].

Scarfing repair process consists in replacing, by bonding, the damaged parent material (original component) with new and mechanically functional material (patch). The quality of the bonded repair depends by several factors: parent and repair materials, surface treatments, adhesive type, curing conditions, joint design. These factors are accurately evaluated and designed, in order to guarantee an adequate stress distribution in the repaired region [26]. According to Katnam et al. [1], the entire process consists of six steps: a) damage assessment; b) material removal; c) surface preparation; d) patch fabrication; e) design; f) monitoring and automation. The first step of the repairing process is the damage assessment (position, type, size, aspect ratio, depth and orientation) using non-destructive techniques such as ultrasonic techniques, thermography, Shearography, etc. in order to evaluate the type and accurately measure its location and extension. In case of non-critical damage with limited extension, the component can be saved and repaired, and several technological evaluations are addressed in order to successfully restore the strength and stiffness of the damaged component [3]. Other required information for repair operations are related to the component manufacturing, such as type of fibre, fibre content, fibre orientation and matrix material, ply sequence, etc.

Considering damage position, depth and extension, the parent material of the composite component can be removed and replaced with a patch, ensuring a complete restoration of the part and its mechanical properties, like strength, stiffness, and stress transfer capability between patch and parent material. This is achieved through an adequate design of the scarf pocket and of the bonded patch. This step is very important and it should be performed by specialists through a mechanical analysis aimed to predict the structural response of the bonded patches and the overall repaired component. This analysis takes into account both material properties and process parameters and it is usually performed by numerical FEM (Finite Element Methods) analysis, fracture mechanics methods, FEM combined with statistical and probabilistic methods, numerical analysis based on multi-scale approach or calibrated and validated experimentally [1].

The main issues of bonded scarf repairs are mainly related to the scarfing geometry, precision and bonding technological parameters. Regarding the scarfing geometry, an adequate scarf angle implies the removal of a large quantity of undamaged material, aiming to avoid delamination damages in parent material. Important bonding parameters are mostly related to the surface curing (treatment pressure and temperature) [28]. These issues are still challenges for repair techniques of CFRP [1].

The machining can be performed manually by a skilled operator (scarfing) or through more accurate CNC machine tools and robots (scarfing or milling). The automation of the scarfing process has been addressed by other studies [29–32]. The result is a tapered pocket with adequate depth to completely remove the damage. The pocket bottom extension (offset from the damage) and pocket sidewalls are characterized by a scarf angle, which represents a very important parameter for the efficiency of the mechanical restoring of the part. Its value depends on several aspects, but a typical taper ratio value is 1:20; other typical values are 1:50 and 1:100 [34–37]. Fig. 1 shows the on-site operations of the machining process.

Since the amount of material to be removed from the original component depends not only on the damage features but also on the geometrical parameters of the designed patch, in the repair design an important step is the optimization. The shape and the scarf angle of the patch should be optimized [33] in order to minimize the undamaged material to be removed which also results in a reduction of machining and repairing time. The choice of the repair surface shape should also take into account other aspects as curvature of the component and other structural constrains such as presence of local reinforcements, edges, thickness changes, bolted joints, etc. In some cases the repair surface belongs to a local planar region without constrains, the scarf angle can be constant and the scarfing surface can be flat and simple such as circular or elliptical for low and high damage aspect ratio respectively. These latter shapes are considered "standard" and effective geometries

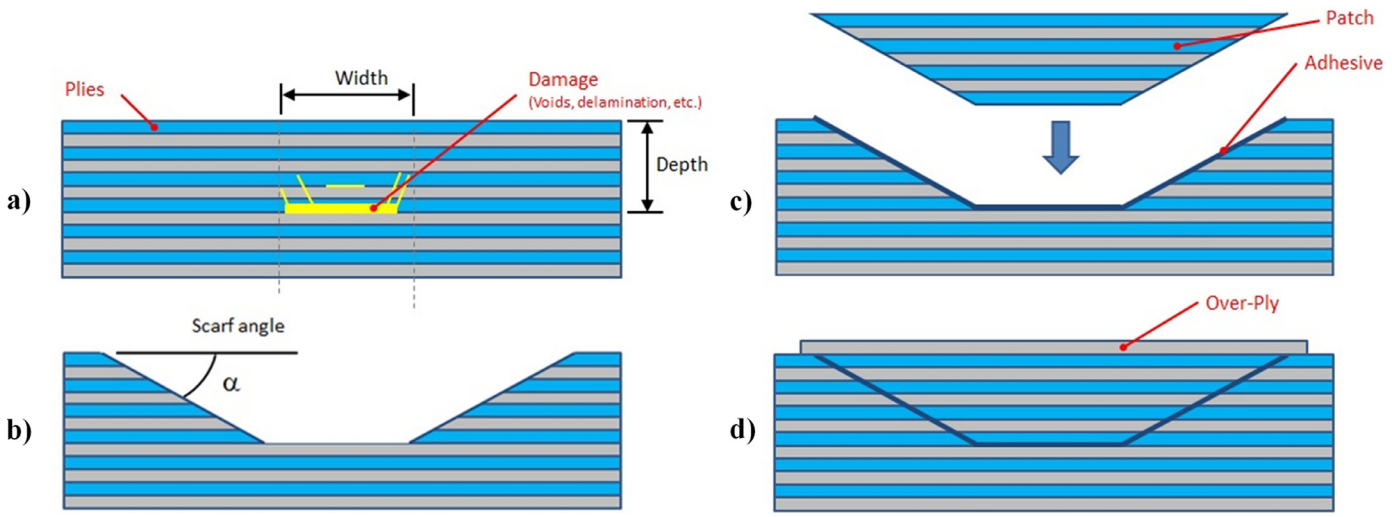

Fig. 1. Repair scheme: a) Damage assessment; b) Material removal; c) Patch bonding; d) Repaired part.

for simple repairs and does not require complex tools to generate the toolpaths [33]. More often, the repair surface must assume curved and irregular shapes (i.e. Non-Uniform B-Spline NURBS surfaces) due to the component geometry and structural constrains and these circumstances increase significantly the complexity of toolpath generation and machining process. Therefore the toolpath generation can be a complicated task which requires specific numerical tools (i.e. CAD/CAM software). More details about the scarfing strategy and machining are presented in Section 7.2.

The material removal can be also performed with unconventional technologies such as laser and abrasive waterjet machining. When the material removal is completed, machined surfaces are prepared through cleaning and activation treatments. Cleaning is aimed to remove CFRP particles, dust and debris generated by the previous cutting process, whereas the activation is done by means of the deposition of a thin film of solvent, improving interface adhesion in the bonding of the patch with the machined pocket. The solvent has also a degrease action, performing an additional cleaning of the surfaces. Plasma and laser treatments are other implemented technologies for cleaning and activation.

The subsequent phase of the process is patch fabrication, which consists of a positive geometry replication of the previous machined pocket. Two different types of patches are known in the state of the art: soft and hard patches [1]. In the present paper, the repair process is referred to large components characterized by thick walls cross-section and a large amount of laminated plies. For this reason, only hard patches are considered [38].

The patches can be molded or machined [1]; the most reliable and accepted in manufacturing context is based on a 3D geometrical modeling of the patch and a CNC milling starting from a workpiece made of well-designed composite plies. The 3D model can be obtained by means of the model of the component and specific measures of the machined pocket but it can be created more accurately by a 3D scanning of the machined pocket. In this latter case a structured light vision system or other 3D scanning technologies can be applied to create the digital geometry reconstruction of the machined pocket. When the patch is ready, it can be bonded to the component into the prepared machined pocket. Final lamination steps are aimed to restore the continuity between parent component and the bonded patch, involving lamination process design, monitoring and automation.

3. Robot requirements

In this section, technical specifications for the robot design are reported. Table 3 summarizes the requirements individuated for the design of a mobile scarfing robot, as well as the related solutions implemented in the architecture hereafter presented in this work.

3.1. General requirements

The aim of the study is to obtain a “semi-autonomous” robotic solution capable of performing all the on-site tasks proper of a CFRP defect reparation. This includes:

- defect detection;
- scarfing and material removal;
- hard patch geometry reconstruction and fabrication;
- solvent application for cleaning;
- machining results data collection;
- application of the patch;
- repair data collection.

Since the hard patch geometry reconstruction and fabrication are carried out “off-line”, they are not intended to be performed by the robot. This study of a first robotic concept is particularly focused on the scarfing and solvent application tasks, representing the defect removal stage; as a further feature, the possibility of performing the inspection phases is considered. Due to the variety of tasks, a fleet of different robots, or a multi-purpose customized single robot is required.

The supervision of the operator is necessary, due to the high cost of the components to be machined. This is the reason why a full automatic solution should be avoided. According to this, the necessity of a real-time inspection device arises.

In order to realize a prototype capable of operating in a wide range of structures, the inner structure of a generic horizontal stabilizer of a commercial aircraft has been considered. These parts are characterized by very narrow tunnels, challenging to be explored and repaired along the whole length. In these tunnels there are no changes in direction; due to this, the steering capacity required is minimal. Furthermore, the forward motion speed can be slow, as all the operations to be carried out do not require fast advancement.

3.2. Dimensions and envelope

The tunnels characterizing inner structures of aeronautical parts are generally trapezoid-like, determined by the external structure shape. In this study a generic tunnel shape and size are considered, as shown in Table 2; the distance between root and tip, corresponding to the length of the stabilizer, is 12 m.

In the definition of dimension constraints, the following conditions

Table 2
Horizontal stabilizer internal tunnel reference shape and dimensions.

	Section	A [*mm*]	B [*mm*]	C [*mm*]
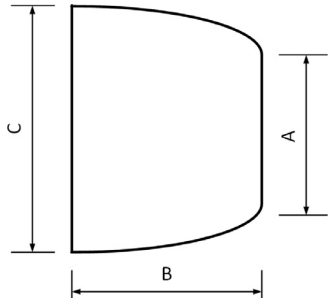	Root	300	274	317
	Tip	135	127	143

need to be considered:

- along the longitudinal direction of the tunnels, there are no obstacles and there are no change in direction;
- the required operation range from the access point, corresponding to the length of the structure, enables the possibility of a tethered solution, as the robot can be fed by ducts and cables, with power supply and necessary fluid tank located outside the tunnel;
- the length of the tunnel is much higher than transversal dimensions, allowing to neglect dimensional constraints in robot design in the longitudinal direction (called “longitudinal design” in Table 3);
- looking at the section shape shown in Table 2, it can be highlighted that an optimized mobile unit should be adaptable to roll angle, in order to avoid interference between the superior edges of the robot and sidewalls. Due to this, the introduction of an internal degree of freedom (“roll disconnection” in Table 3) allows a better exploitation of the available clearance.

3.3. Machining requirements

As per the device proposed in [5], machining a scarfing pocket on a defined surface requires tool mobility and control along 3 axes. However, the aim of a mobile robotic solution is to repair the defects in any position along the inspected component; due to this, the end-effector shall be able to reach any point of the structure, even corners, and perform scarfing operations also in tilted configurations. According to this, the mobile robot has to be capable of machining controlling the motion along 5 degrees of freedom. Regarding machining parameters, the following technical specifications have been considered:

- Cutting speed. A reference value of this parameter is 6000 rpm which is the cutting speed of manually driven tools.
- Machining depth. High cutting forces can results in component damages (i.e. typically ply delaminations). For this reason, it should be limited to a safety threshold. Since cutting force is tightly related to machining depth, the maximum machining depth is fixed to h_{max} = 0.1 mm. This value guarantees the preservation of the component integrity, since that a small portion of material is removed at each scarfing step.
- Cutting force. According with the previous parameter, in order to find a safety threshold value, the force applied to perform the machining of a depth h = 0.1 mm of CFRP has been experimentally measured in manual scarfing operations. Measurements showed that it does not exceed the value of 30 N. It is worth to note that this value is overestimated compared to the ones reported in [39], in which the cutting force in grinding operation on CFRP is measured and the relationship between cutting parameters and quality of machining, in terms of roughness and accuracy, is investigated. However, in order to comply with occasional demanding working conditions, the target has been set to the value of 30 N.

Table 3
Robot specifications and design solutions

Requirements	Expected performance	Design solution/s
Tasks to perform	Inspection, scarfing machining, cleaning, solvent application	Single modular mobile robot
Level of automation	CAM-programmed machining; “jogging” positioning enabled	Semi-automated solution, on-board camera
Working distance	Up to 10 meters in straight direction	Tethered robot
Auxiliary resources	Electrical energy, pressurized air, fluids for cleaning	Off-board provided by a single duct
Additional requirement	Machining waste removal, direct image acquisition	On-board vacuum device, on-board camera
Positioning dexterity	Steering not required; transversal displacement enabled	Fixed axes omni-wheeled robot, active lateral rods
Envelope	Explore narrow tunnels with undefined quadrilateral section	“Longitudinal design”; internal “roll disconnection”
Degrees of freedom	5 for machining; 3 for in-plane positioning	Combine 1 machining and positioning DoF
In-plane positioning	Torques and velocities not demanding (slow dynamics); accuracy 1mm	Longitudinal position: externally referenced sensor; transversal pos. and orientation: redundancy (4 rods)
Machining	Cutting force F = 30 N; S = 6000 rpm; Maximum scarfing depth h_{max} = 0.1mm; depth accuracy 0.02mm; in-plane accuracy 1mm.	Pneumatic motor for machining; displacement sensor in proximity of the milling tool for precise depth measurement

Scarfing chips have to be removed during machining, suggesting the necessity of a vacuum system onboard. Moreover, in order to increase scarfing and repair quality, a high-precision measuring system can be used to acquire the machined depth and the pocket walls profiles. Such a sensor enables a closed-loop control for the machining process. Although higher precision is required to machined depth, the external shape of the machined ply portions is less demanding, as the repairing patch is then realized accordingly to the final shape of the machined pocket; due to this, the required accuracy is 0.02 mm for machining depth, and 1 mm for in-plane positioning and machining.

4. Concept and design

The survey of the state of the art reported in Section 1 highlights the following design choices:

- a mobile robot working in narrow spaces can be tethered or untethered;
- the locomotion subsystem can be realized by a crawler vehicle, or by arms equipped with traction wheels pushing upon the tunnel side walls;
- the robot architecture can be symmetric or asymmetric;
- a large variety of sensors to scan the inner surface of the tunnel is available.

In order to develop a new, task-oriented design, the tasks listed in Section 3.1 are analyzed with a functional design-oriented approach, illustrated in Fig. 2 by means of the Idef0 convention. The schematic reported in the figure clearly highlights the advantages of a modular approach: several tasks, indeed, share the following resources (intended as the means necessary to carry out the activities) or controls:

- "Motion": includes both "Rapid Motion" of the robot or "Fine 5 DOFs (degrees of freedom) Positioning" of the tool.
- "Energy": electrical power and pressurized air.
- Sensors: micro camera or displacement sensor.

Moreover, the different tasks are necessarily sequential and cannot be performed simultaneously, furtherly validating the modularity as the optimal solution.

Fig. 3 shows the whole robotic system; the length of the tunnel is exploited to distribute the robot units and components. The following modules are highlighted and described in the following paragraphs:

- Rover;
- Arm;
- Scarfing Forearm;
- Cleaning Forearm;
- Semi-trailer.

4.1. Rover

The Rover is the main component of the robotic system. It tows the Semi-trailer through a rear connector, whereas the Arm is connected on its front side. With reference to Fig. 4, the rover subsystems are here described.

Aiming to the global optimization of the on-board actuation

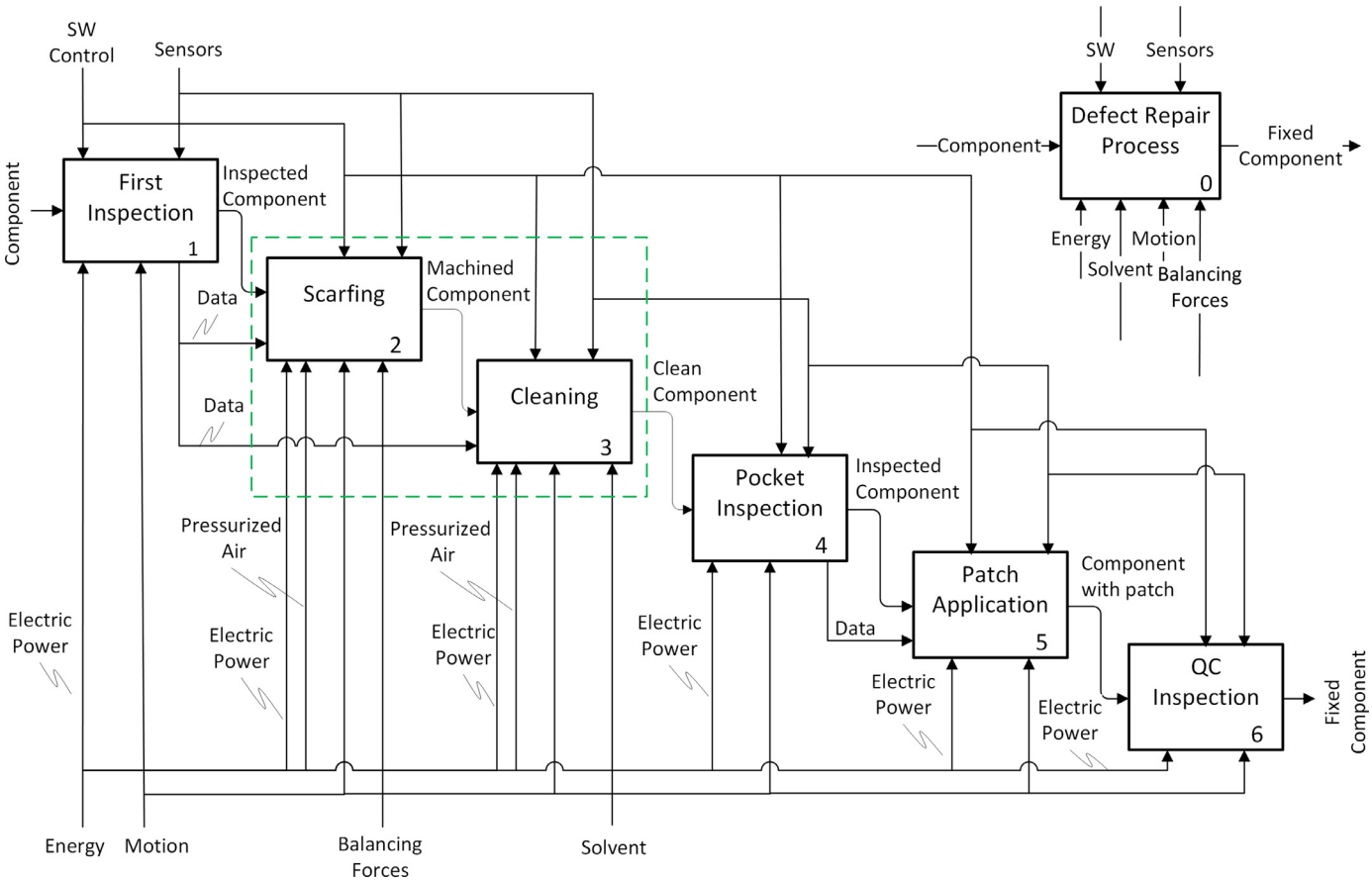

Fig. 2. Representation, according to Idef0 standard, of the Defect Repair Process.

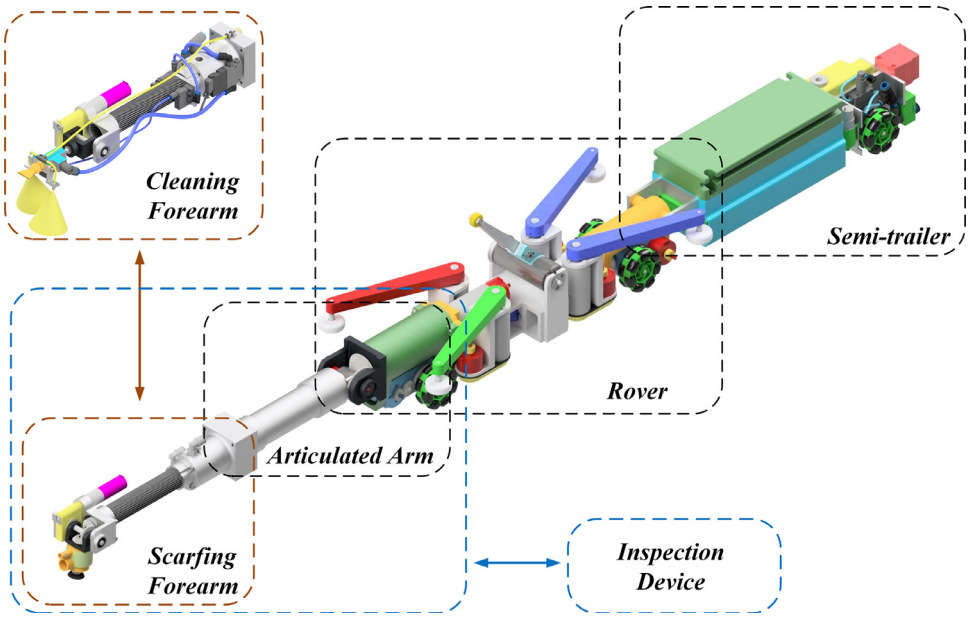

Fig. 3. The robotic system with the scarfing forearm mounted. Up-left corner: the cleaning Forearm.

systems, the “traction” motion is exploited also as the first DOF during the machining task. It follows that an optimal concept for the Traction subsystem is essential for robot effectiveness. Different locomotion mechanisms are available, either from vehicles technology, either from biological systems [40]. In particular, crawl (longitudinal vibration) does not fit our requirements, because does not guarantee a constant speed, essential during the scarfing process. Sliding (transversal vibration) requires free lateral gaps, not available in proximity of the tapered tight section (wing tip). Since similar drawbacks apply to walking systems, a wheeled mobile robot represent the most appropriate solution. In order to avoid traction slip effects, better distributing the traction force on the component surface, the subsystem is composed by two identical units, a front one and a rear one, each one consisting of a servomotor (with relative encoder and gearhead) and a couple of wheels, connected through an external gearbox. The implementation of “Omni-directional” wheels enables passive transversal movements.

The Pushers subsystem consists of four lateral and one upper aluminum balancing rods, directly controlled by dedicated servomotors. The lateral pushers have a double functionality: control transversal position and yaw angle of the Rover, and balance machining forces in the horizontal plane. It follows that the Rover itself controls the 3 DOFs describing the position of the robot in the horizontal plane. The upper pusher purpose is to maintain the horizontal pose of the robot, balancing vertical machining forces. In order to reduce friction with tunnel walls, that would obstruct longitudinal motion, pusher tips are equipped with rollers.

Each traction subsystem is connected to rover frame with a relative rotational DOF, allowing the Active suspension subsystem to compensate roll movement, directly acting on them: according to the slope measured by an on-board inclinometer, one traction subsystem is rotated by a servomotor in order to maintain the frame in a horizontal pose, even in case of curved supporting surface. The second traction

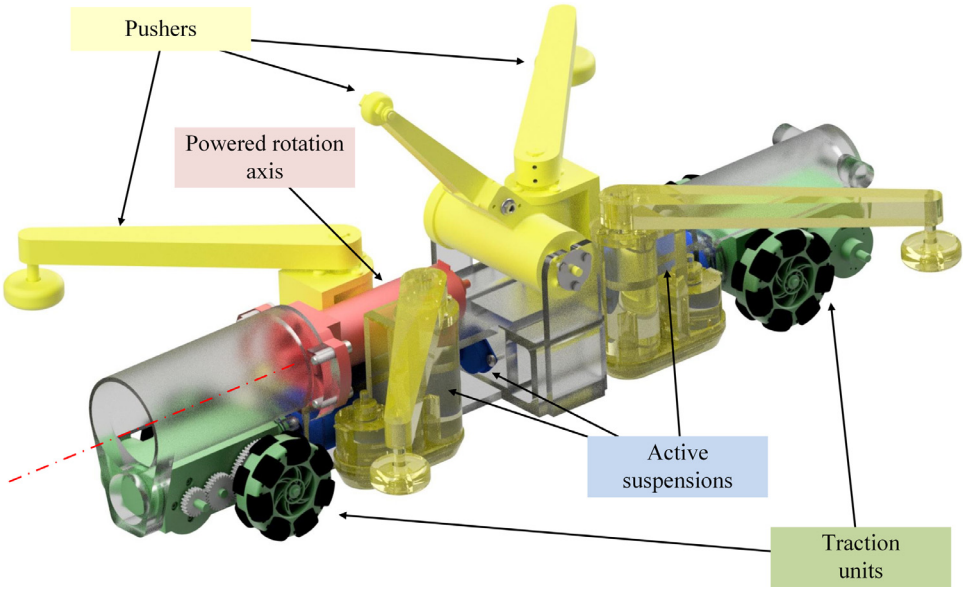

Fig. 4. A rendered illustration of the Rover, with its subsystems highlighted with different colors: traction subsystem in green; pushers subsystem in yellow; active suspensions subsystem in blue; horizontal rotation axis in red. (For interpretation of the references to color in this figure legend, the reader is referred to the web version of this article.)

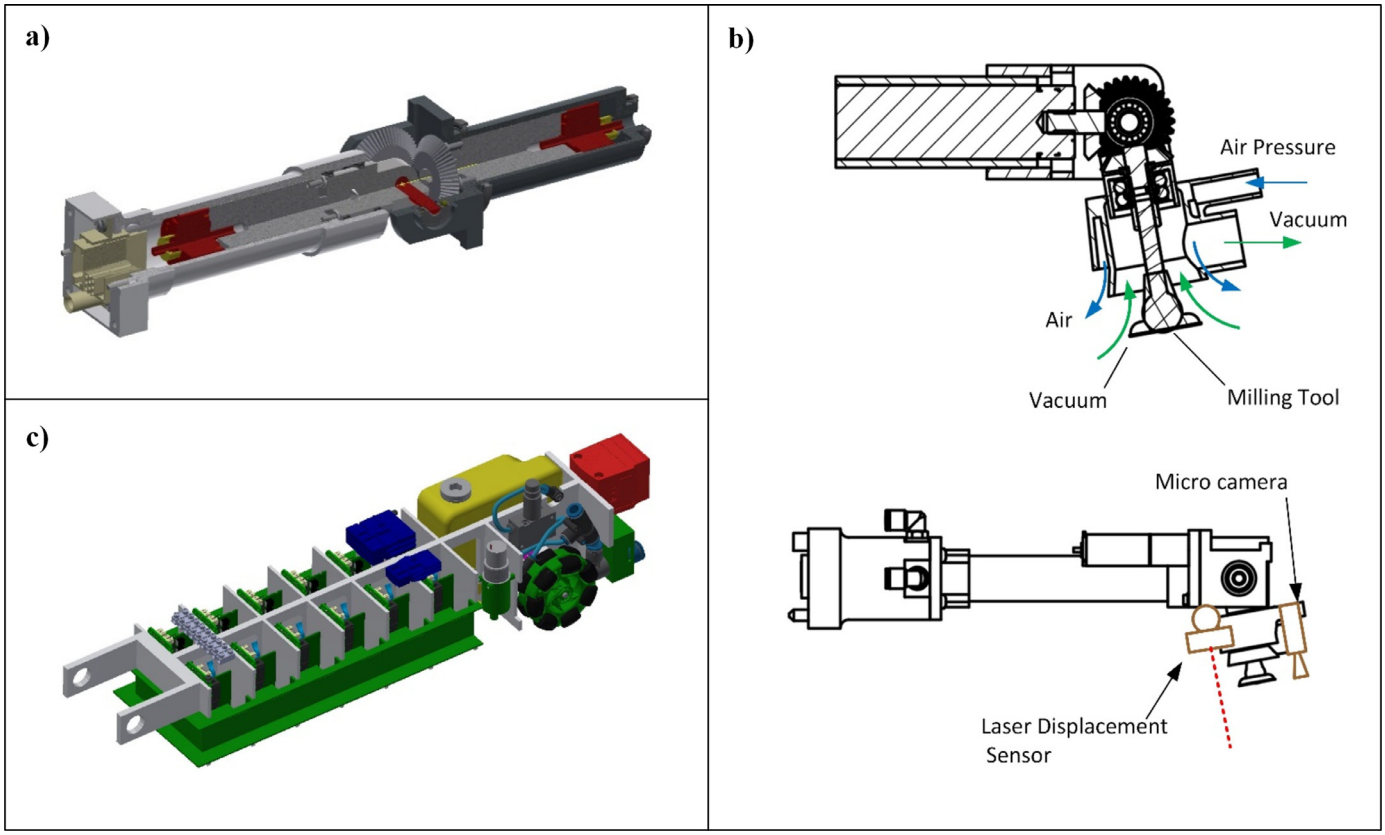

Fig. 5. Details of the robot: a) Transversal section of the Articulated Arm, b) Schematic representation of the Scarfing Forearm with the relative instrumentation and c) The Semi-trailer, hosting the auxiliary services.

subsystem is free to rotate and consequently complies with the rotation imposed to the other one. The issue of inclined or curved surface is very common for aeronautical components.

The Rover hosts an active Horizontal rotation axis, with the relative servomotor. It is used, with modular logic, either in the inspection process to rotate a customized 3D scan system, either to realize the first rotation of the spherical joint of the Arm, described in the following section.

4.2. Articulated arm

The Arm is composed by a spherical joint on its root, a rod and a tool changer on the tip. The spherical joint consists of three actuated revolute joints. The first one is installed on the Rover, the other ones are directly integrated into the arm carbon fiber tube, as depicted in Fig. 5(a).

The manual tool changer integrates also the electrical contacts for signals and energy transfer between the Arm and any Forearm installed. The tool changer, indeed, enables the use of the robot for both, scarfing and cleaning processes. Both the relative forearms are equipped by a further servomotor, controlling the last revolute joint of the arm kinematic chain (tool tilt). This is to optimize the whole arm design considering the narrow space available inside the tunnel.

4.3. Scarfing forearm

The Scarfing tool includes a pneumatic grinding motor, a revolute joint (corresponding to the tilting movement of the tool), a mechanical power transmission, a tool holder, a vacuum cuff and sensors. Fig. 3 illustrates the Scarfing Forearm installed on the robot. The grinding motor is a two stages air vane motor, expressly designed for grinding operations. The installed power is 250 W with a speed (idling) of 32000 rpm. It is embedded in the forearm tube to optimize the whole design.

In order to remove the dust generated during machining, a customized vacuum cuff was designed. This component is critical because it must be efficient and small at the same time. As shown in Fig. 5(b), the vacuum cuff is composed by two air chambers: the external one is pressurized to create an “air curtain”, while the inner one is a vacuum chamber to collect the dust. In this way, dust spread is prevented and device efficiency is increased. On the tip, a micro-camera and a laser displacement sensor are equipped. The micro camera is useful to inspect the scarfing process, either in real time or in post-processing mode, whereas the displacement sensor measures the depth of the scarfed pocket.

4.4. Cleaning forearm

The Cleaning Forearm, shown in Fig. 3 as an alternative to the Scarfing Forearm, includes the following subsystems:

- an air compressed line with an air nozzle to clean the machined surface and to dry the cleaning solvent;
- solvent nozzles and their fixture;
- a camera to monitor the cleaning process.

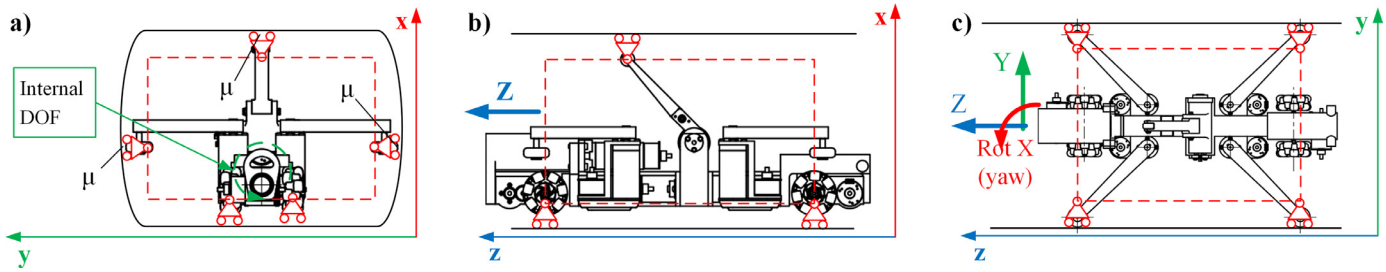

Fig. 6. DOFs of the Rover in the three planar views.

Hoses, electro valves, fittings and any other element needed to feed air and solvent to the nozzles are installed on board.

4.5. Semi-trailer

The auxiliary equipment is mainly installed on the semi-trailer, connected to the rear side of the Rover. As shown in Fig. 5(c), the following services are included:

- an insulated compartment for 12 digital miniaturized electrical drives;
- a tank for the solvent used in the cleaning process;
- electro valves and hoses for the solvent circuit;
- connectors for electrical power, air pressure, control signals and video.

It also hosts Laser displacement sensor, in its rear part, to detect the longitudinal Rover position inside the tunnel as will be further explained.

As pointed out in Section 1, robot working into narrow spaces can be tethered or untethered. The tethered version is definitely preferred for this application; beyond the space saving and the dimensional advantages for robot design, it guarantees that the robot can be extracted from the tunnel, in every situation (i.e. power blackout or control system failure). The umbilical cord, attached to the Semi-trailer, feeds electrical power, air pressure, networking, auxiliary electrical signals (i.e. emergency stop or control dedicated lines), a video cable for the inspection camera and a steel rope to extract manually the robot from the tunnel in emergencies. The other extremity of the umbilical cord is connected to a power cabinet and a control system.

5. Kinematic analysis

In this section, the kinematics of the whole robotic system is analyzed. The first paragraph describes the architecture, in terms of degrees of freedom of the robot; the other two paragraphs describe Rover and Arm kinematics.

5.1. Degrees of freedom

As hypothesis for the kinematic analysis, the Rover is considered as a rigid body and always in contact with the lower surface of the aeronautical component. As evident in the three planar views shown in Fig. 6, it has three planar DOFs: two translations and one rotation (yaw). The internal DOF introduced by the active suspension is neglected in this analysis, but it allows to keep the Rover lying on a horizontal plane regardless to ground surface imperfections or slopes.

Fig. 7 shows the robot in a generic pose with respect to a reference side wall. The DOFs of the whole robot are individuated as follows:

- The Rover longitudinal motion represents the 1st DOF (translational along $\hat{\mathbf{z}}_0$);
- 2nd and 3rd DOFs of the Rover (respectively, transversal translation along $\hat{\mathbf{y}}_0$ and yaw rotation around $\hat{\mathbf{x}}_0$) are not used in the scarfing and cleaning processes, in order to simplify the control system. They are instead used to move the whole robotic system in the tunnel for the inspection process and for fast position adjustments;
- The 4th DOF is the first of the spherical joint at arm root;
- The 5th and the 6th DOFs complete the spherical joint.
- The 7th DOF (not represented in the figure) is represented by the tool tilt rotation, realized by each Forearm module.

Table 4 summarizes the DOFs activated for each operation mode: Rapid Motion (RM) for in-plane robot advancement, or Fine Positioning (FP) used for scarfing and cleaning operations. In this latter case, as per the initial requirements, a 5 DOFs machining is replicated, although the remaining 2 DOFs can be used occasionally to restore the whole robotic system position. Rover and Arm kinematic analyses, hereafter described, correspond to the kinematics involved respectively in Rapid Motion or Fine Positioning operational modes.

With reference to Fig. 7, description and dimensions of the variables are listed in Appendix B.1. The main aim of the direct kinematic analysis is to express the position and orientation of the Rover in the $\mathbf{O_0}$ frame (operational space), known the values of joint variables, measured by encoders or external sensors. For the Rover, joint variables are represented by the four angles β_i of the pushers, in contact with side walls, and the two angles δ_i of the traction axles. A set of six joints variables is so defined, but the following considerations apply:

- The positions of a set of two pushers on the same side of the robot is sufficient to univocally define $o_{1,y}$ and α; the position of the opposite pushers is adjusted accordingly. In this analysis, β_2 and β_3 are the independent variables, as they interface with the chosen reference wall side.
- A single variable is sufficient to define the longitudinal translation, indeed it can be reasonably assumed $\delta_1 = \delta_2$; on the other hand, the laser measured d_{msr} provides a more precise position, as the integration of servomotor encoder data would be strongly affected by slip effects.

The vectors $\mathbf{q}_R = [\beta_2\ \beta_3\ d_{msr}]^T$ and $\mathbf{p}_R = [o_{1,z}\ o_{1,y}\ \alpha]^T$ express respectively the coordinates of the Rover in the joint space and in the operational space. Direct kinematics Equations set (1) allow to obtain operational coordinates $\mathbf{p}_R$, by joint variables $\mathbf{q}_R$, measured by the

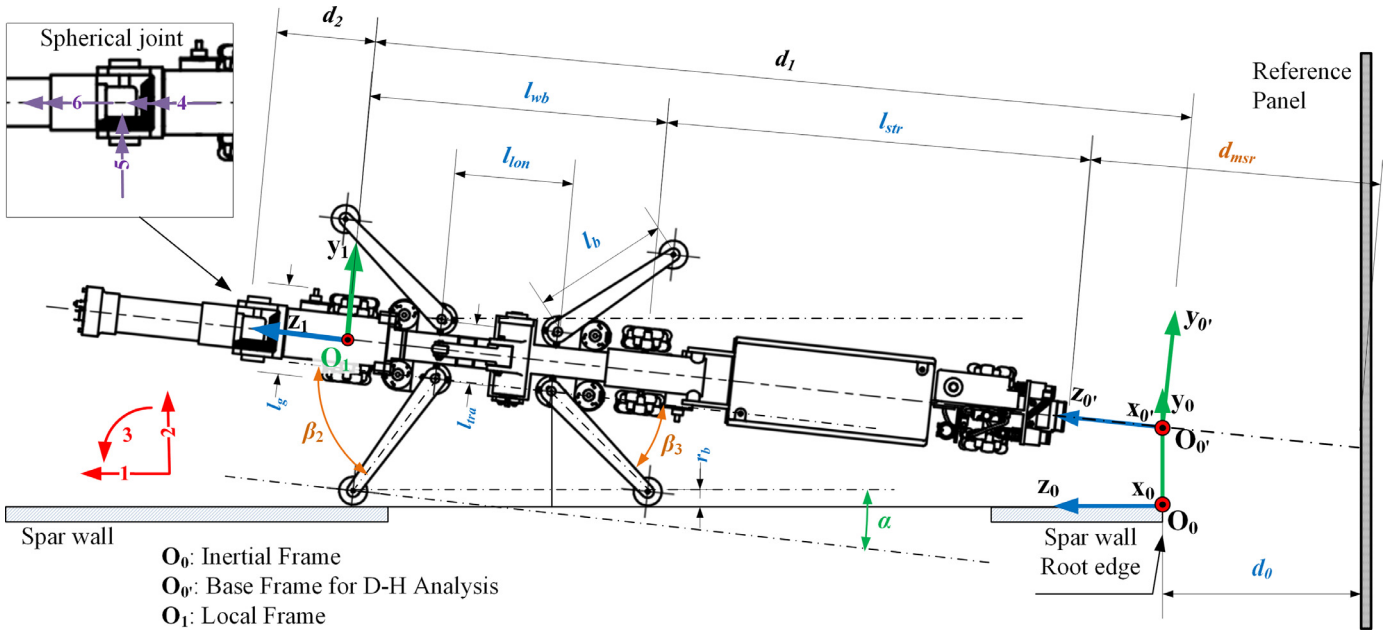

Fig. 7. Top schematic view of the architecture: DOF_R are indicated in red, geometric parameters used for Rover kinematics in blue, coordinates in joint space in orange and in operational space in green (position of O_1 and orientation α). Spherical joint axes are detailed in purple. (For interpretation of the references to color in this figure legend, the reader is referred to the web version of this article.)

Table 4
Rover and Arm DOFs (respectively, DOF_R and DOF_A) involved in Rapid Motion (RM) or Fine Positioning (FP) modes.

DOF_R	DOF_A	Function	RM	FP
1		Translation along $\hat{\mathbf{z}}_0$	1	1
2		Translation along $\hat{\mathbf{y}}_0$	2	–
3		Rotation around $\hat{\mathbf{x}}_0$	3	–
	4	Spherical joint I axis	–	2
	5	Spherical joint II axis	–	3
	6	Spherical joint III axis	–	4
	7	Forearm tilting	–	5

encoders of two involved servomotors and the rear laser sensor, onboard.

$$\begin{cases} o_{1,z} &= (d_{msr} + l_{wb} + l_{str})\cdot\cos(\alpha) - d_0 \\ o_{1,y} &= l_p\cdot\sin(\beta_2 - \alpha) + \frac{l_{lon}}{2}\cdot\cos(\alpha) + r_p \\ \alpha &= \arctan\left(\frac{\sin(\beta_2) - \sin(\beta_3)}{l_{lon}/l_p + \cos(\beta_2) + \cos(\beta_3)}\right) \end{cases} \quad (1)$$

In closed-loop control systems, both direct and inverse kinematics equations are necessary; therefore, inverse kinematics is defined by the Equations set (2).

$$\begin{cases} l_{msr} &= \frac{o_{1,z} + d_0}{\cos(\alpha)} - l_{wb} - l_{str} \\ \beta_2 &= \alpha - \arcsin\left[\frac{1}{l_p}\cdot\left(r_p - o_{1,y} + \frac{l_{lon}}{2}\cdot\cos(\alpha)\right)\right] \\ \beta_3 &= -\alpha - \arcsin\left[\frac{1}{l_p}\cdot(l_{lon}\cdot\sin(\alpha) - l_p\cdot\sin(\beta_2 - \alpha))\right] \end{cases} \quad (2)$$

5.2. Arm kinematics

The kinematic study is carried out with the standard Denavit-Hartenberg (D-H) convention [41]. Fig. 8 shows the link frames oriented as per D-H convention; the table reports relative parameters, with joints variables highlighted in orange. Resulting relations of direct kinematics are described by the following matrix equation:

$$\mathbf{A}_{05}(d_1, \vartheta_2, \vartheta_3, \vartheta_4, \vartheta_5) = \mathbf{A}_{01}\mathbf{A}_{12}\mathbf{A}_{23}\mathbf{A}_{34}\mathbf{A}_{45} \quad (3)$$

with each $\boldsymbol{A}_{ij}$ representing the frame transformation matrix between frame i and frame j. $\mathbf{A}_{05}$, which extended expression is reported in Appendix A, is composed as follows:

$$\mathbf{A}_{05} = \begin{bmatrix} \hat{\mathbf{x}}_5 & \hat{\mathbf{y}}_5 & \hat{\mathbf{z}}_5 & \mathbf{p}_e \\ 0 & 0 & 0 & 1 \end{bmatrix} \quad (4)$$

The extended matrix expression is reported in Appendix B.2. Operational variables are represented by machining tool position $\mathbf{p}_e$ (corresponding to the position of $\mathbf{O}_5$ in the inertial frame) and its orientation. Due to the robot architecture, the pose of the tool is univocally defined by only two angles; according to Eulerian angles standard, indeed, it is never subjected to yaw rotation. They can be obtained comparing the first column of Eulerian angle matrix with $\hat{\mathbf{x}}_5$. Therefore, the set of operational coordinates is defined by the vector $\mathbf{p}_{Arm} = [p_{e,x}\ p_{e,y}\ p_{e,z}\ \Theta\ \phi]^T$, with Θ and ϕ respectively pitch and roll Eulerian orientation angles.

The Arm inverse kinematic problem is a non-trivial problem and solved with a standard approach [42]. The resulting relations, defining D-H joints variables as function of operational variables, are reported in Appendix B.3. As a formal note, although Rover and Arm kinematics are treated separately, analyzing Fig. 7 the relation between the variables of the two problems can be obtained:

$$\begin{aligned} d_1 &= d_{msr} - \frac{d_0}{\cos\alpha} + l_{wb} + l_{str} \\ &\text{with} \alpha = \alpha(\beta_2, \beta_3) \end{aligned} \quad (5)$$

6. Control strategy

This section, concerning the robotic system control strategy, is focused on the following topics:

- high level logic control diagram of the whole robotic system;
- high level control diagram of the Articulated Arm;

O_i	ϑ_i	α_i	a_i	d_i
O_1	0	0	0	d_1
O_2	ϑ_2	90°	0	d_2
O_3	ϑ_3	90°	0	0
O_4	ϑ_4	90°	0	d_4
O_5	ϑ_5	0	a_5	0

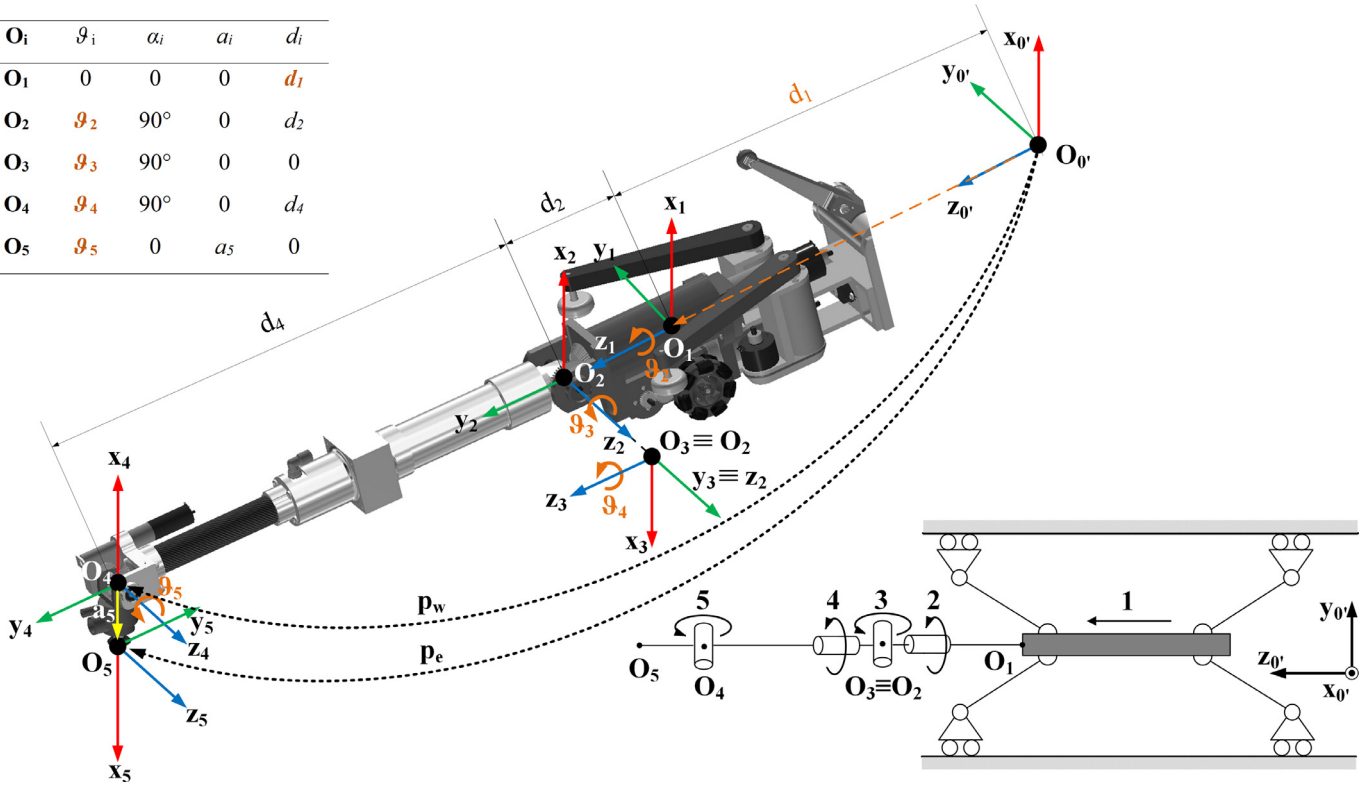

Fig. 8. D-H Frames and Parameters, corresponding to the "Fine Positioning" DOFs.

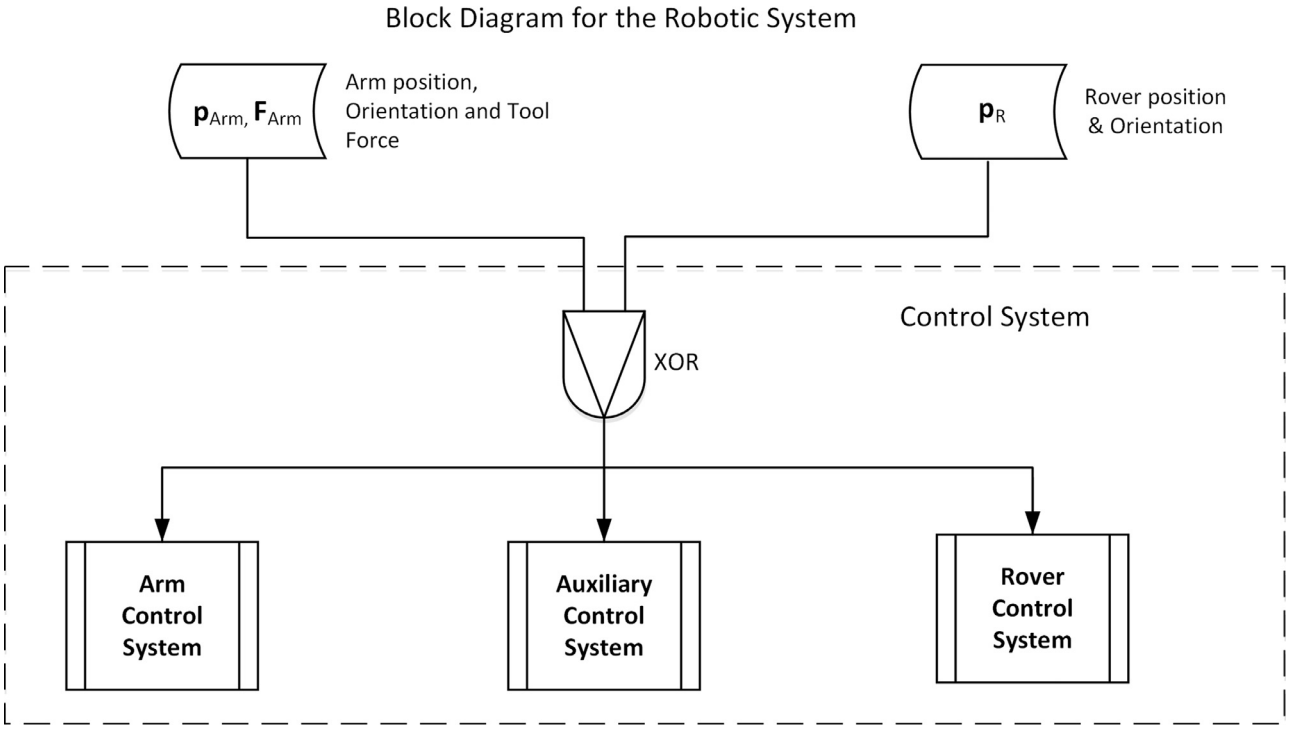

Fig. 9. Control diagram for the whole robotic system.

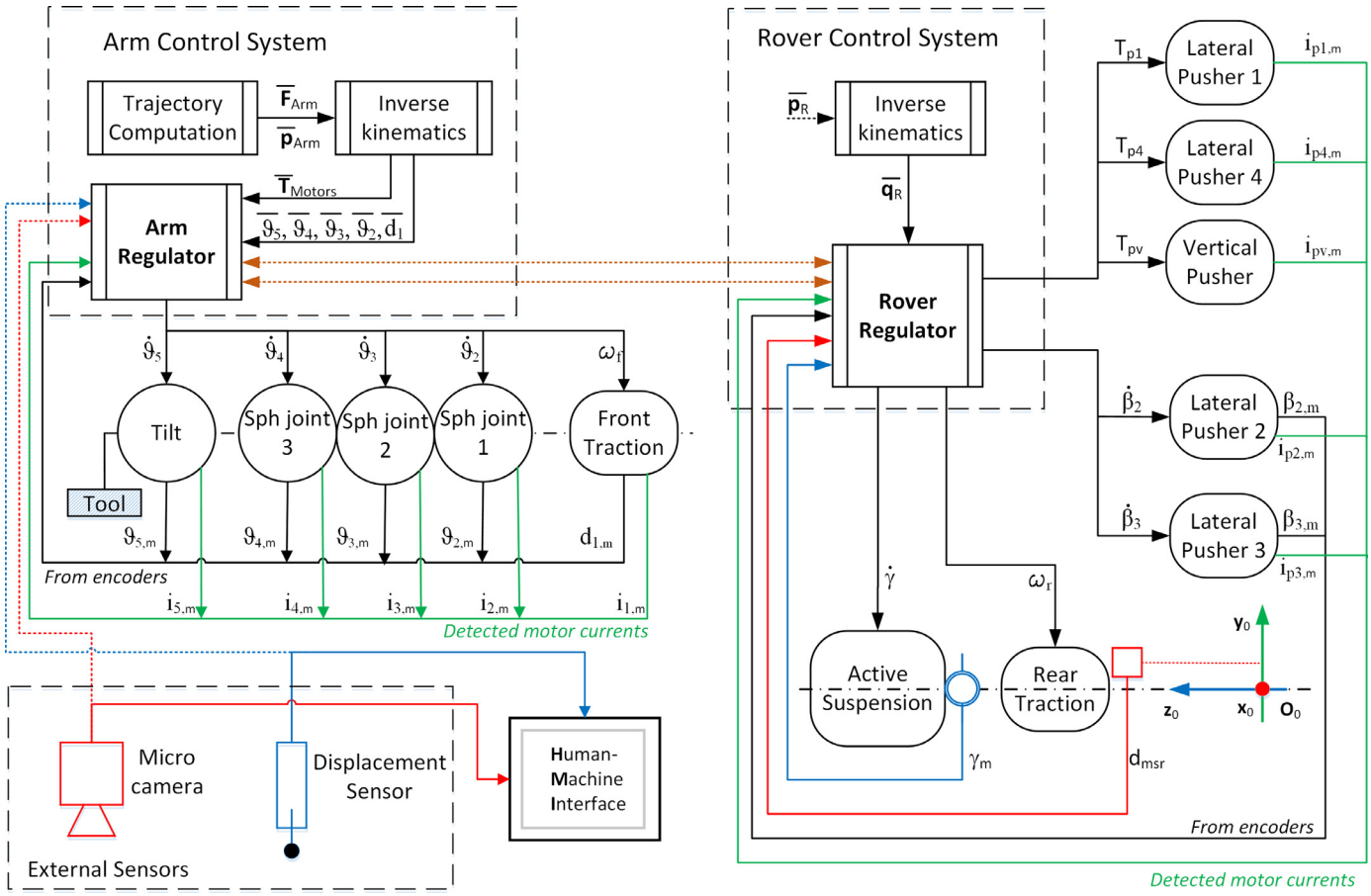

Fig. 10. Control diagram for the Articulated Arm (on the left) and for the Rover (on the right).

- high level control diagram of the Rover;
- procedures for inspection, scarfing and cleaning operations.

6.1. Robotic system control diagram

The general approach to the control system design is shown in Fig. 9. For scarfing and cleaning operations, tool position, orientation and reaction force applied on the tool are inputs of the control system. Alternatively, for the inspection or the Rapid Motion inside the tunnel, Rover operational coordinates $\mathbf{p}_R$ are used. Only one set of coordinates is processed at once; therefore, the provided set automatically enables the relative working mode.

According to robot architecture, the control system is divided in three subsystems: the main ones are the Arm Control System and the Rover Control System, detailed in the following sections. The Auxiliary Control System manages auxiliary fluidic on-board plants (air and cleaning solvent) and monitors sensors data (determining end strokes or emergency stop).

6.2. Control diagram of the arm

The control diagram of the Arm is shown in Fig. 10. By the input data, the inverse kinematic and kineto-static variables are computed and interpolated. The results allow the Arm Regulator to control the Arm. Comparing instantaneous values of positions and currents (proportional to the torques) with the desired ones, the target variables are set according to the errors. Due to the irregular shape of the bottom surface of the aeronautical components considered, the wheels do not roll on a smooth plane, but over a surface featured by small steps. For this reason, the Arm Control System cannot rely only on the tool coordinates to machine the component, but it must control the contact force too, according to experimental laws.

The images acquired by a micro camera and the machining depth measure acquired by a displacement sensor completes the Arm Control System. These information are exploited either by the control system, either by the operator surveilling the process.

6.3. Control diagram of the rover

The Rover is controlled with a logic, also described in the diagram in Fig. 10. This control system works in conjunction with the Arm Control System during scarfing and cleaning, differently from the inspection process and robot Rapid Motion. The Rover Control System implements the following logic to control Rover's servomotors:

- Acquisition of inclinometer data and regulation of the Active suspensions, to keep Rover frame in horizontal pose, in order to avoid interferences between the robot and the component, especially at component tip.
- Control of Rover traction units. The torque is distributed among the two units by supplying them with the same current; on the other hand, only the frontal traction axis is speed-controlled. During scarfing operations, rover traction balances forces in $\hat{\mathbf{z}}_1$ direction (referred to Fig. 7); consequently, its function is executed in connection with the Arm Control System, operating on the frontal axes.
- Balance of the horizontal pushers. The ones on the side of the selected reference side wall (see Fig. 7) are position-controlled, imposing β_2 and β_3, defining Rover position and orientation. The opposite pushers, acting on the other side wall, are force-controlled for robot global stability in the $\hat{\mathbf{y}}_1\hat{\mathbf{z}}_1$ plane.

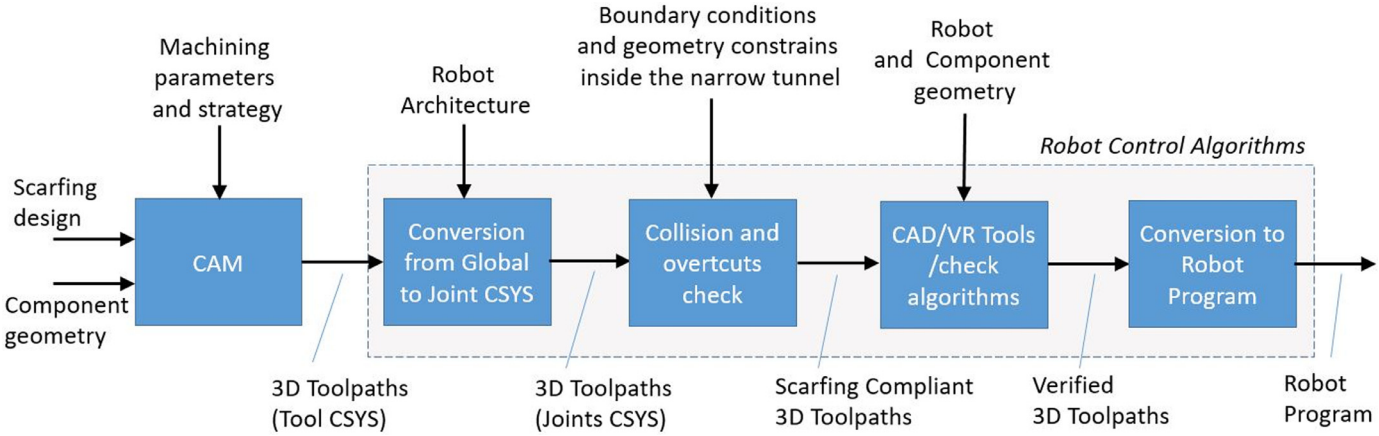

Fig. 11. Scarfing toolpath generation process.

- Control of the vertical pusher, with the aim of applying the minimum force, sufficient for robot stability in the $\hat{x}_1\hat{z}_1$ plane. This action, crucial during machining, is exploited also during Rapid Motion to consequently increase the adherence of robot wheels.
- Acquisition of robot advancement inside the tunnel, detected by the rear displacement laser sensor.
- Control of the vertical pusher, with the aim of applying the minimum force, sufficient for robot stability in the $\hat{x}_1\hat{z}_1$ plane. This action, crucial during machining, is exploited also during Rapid Motion to consequently increase the adherence of robot wheels.
- Acquisition of robot advancement inside the tunnel, detected by the rear displacement laser sensor.

6.4. Inspection operation

For this operation, the installation of a structured-light 3D scan tool with a field of view of 180° is required. Due to the field of view feature, at least two full-length longitudinal scansions are necessary for a complete reconstruction of the tunnel. After the first survey, consisting in the straight motion of the robot along the whole length of the tunnel, up to the tip of the component, 3D Scan tool is rotated and the second acquisition is performed, with the robot moving backward to the root of the component. The merge of the two acquisitions is carried out off-line.

6.5. Scarfing operation

In order to reach the damaged zone, a Rapid Motion is performed, followed by a Fine Positioning step. Scarfing toolpaths are then defined by implemented algorithms (CAM), according to the defect position and depth. By means of this software, the specific manufacturing process is designed in the operational space, and collision-free trajectories are defined. The arm kinematic relations allow to control joints variables (for the machining phase: 1st, 4th, 5th axes to position the tool and 6th, 7th axes to orient it). The on/off turning of the grinding motor is controlled, and the depth of the machined pocket is continuously verified by means of the laser sensor on Scarfing forearm tip.

As stated in Section 2, the scarfing strategy consists on a layer-by-layer removal of material starting from the outer skin of the component. The design of the scarfing is effectively executed with CAD tools starting from the component geometry (solid model), which can be already available or can be obtained by geometry reconstruction systems. When the repair design is complete, the solid model of scarfing pocket is available and it can be processed by a CAM software to generate the 3D toolpaths. The CAM tools basically proceeds with a slicing phase of the model and a definition of all layer plies to be machined with a resolution fixed by the step depth of the scarfing. The obtained trajectories are subsequently processed by the robot control algorithms, in order to generate the joints positions to be executed by the robot, according with the boundary conditions and other geometry constrains, preventing collisions inside the narrow tunnels. Finally, the resulting file is verified and revised to avoid overcuts on each layer and collisions of tool and robot. This latter check can be performed through customized algorithms or by means of a kinematic simulation into a virtual environment such a CAD software or specific virtual reality tools (i.e. CGTech Vericut, Esi IC.IDO).

After the collision and overcuts check, finally the toolpath file is converted into a robot program to perform the scarfing task. The toolpath generation process is summarized in the block diagram showed in Fig. 11.

6.6. Cleaning operation

Even in Cleaning operation two phases are necessary: Rapid Motion (RM) and Fine Positioning (FP). Nevertheless, fine positioning is significantly simplified, as the involvement of the CAM software is not necessary, due to the lower precision required by this operation. The cleaning fluid electro-valves is coordinated with movement during Fine positioning phase.

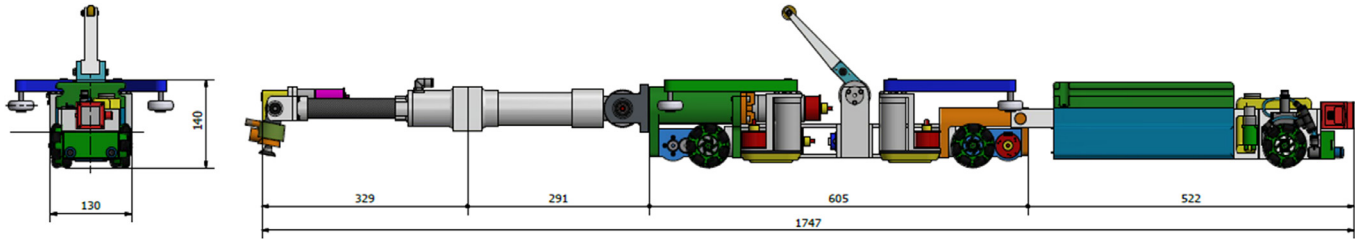

Fig. 12. Main dimensions of the mobile robot.

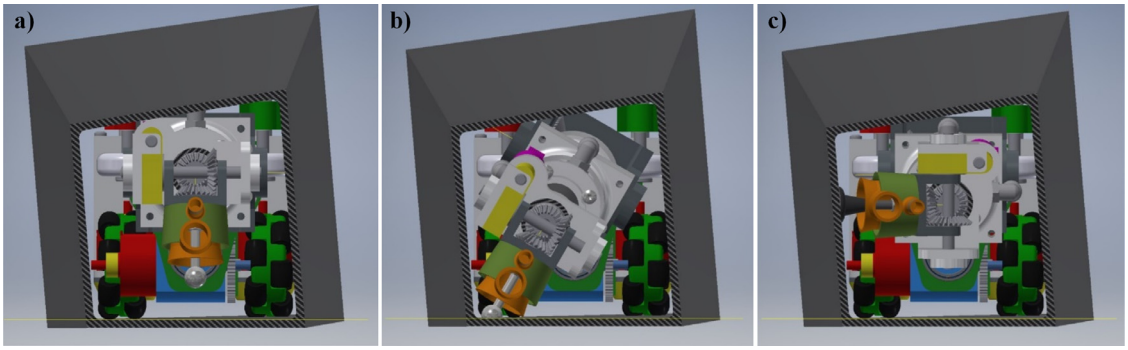

Fig. 13. From left to right: a) the robot in tunnel mid position, at tip extremity, equipped with a spherical milling tool; b) the robot at tunnel tip, scarfing a lower edge of the tunnel, by a spherical mill; c) the robot at tunnel tip, scarfing a lateral edge of the tunnel, using a circular abrasive disk.

7. Discussion

7.1. Architecture

As per the identified requirements, the robot architecture exploits the longitudinal dimension, with a strongly limited transversal envelope, as demonstrated by the dimensions shown in Fig. 12. From a geometrical point of view, the proposed design enables the use of such a robot in multi-spar box CFRP components (wings and stabilizers), as it complies with the demanding dimensions of the tunnels. Moreover, the machining tool is provided by the articulated arm, even thinner than the Rover, as shown in Fig. 13; thanks to this, possible defects in the tip of any component of this type can be easily reached. Although the length of the articulated arm could lead to a lack of dexterity during machining, the robot working principle is unaffected by this feature: exploiting the length of the tunnels, the robot can move forward or backward in order to machine any defect with sufficient dexterity; in this sense, it is also important to highlight the possibility, depending on component size, of exploring the component in both directions.

The robot has no direct steering capability but lateral rods enable transversal translations and the possibility of maintaining a certain orientation with respect to the side wall of the tunnel, identified by parameter α. Theoretically, α is limited by the width of the tunnel w_{tun} in a certain longitudinal position z, and by the dimensions of Rover and Semi-trailer as per Eq. (6), with reference to Fig. 7; however, real practice will require very limited orientations, and the only aim of rotation capability is to ensure the reachability of any point.

$$\alpha_{\max}(z) = \arcsin\left(\frac{w_{tun}(z)}{l_D}\right) + \arccos\left(\frac{l_g}{l_D}\right) - \frac{\pi}{2}$$
$$\text{with} l_D = \sqrt{(l_{str} + l_{wb} + d_2)^2 + {l_g}^2} \tag{6}$$

The proposed design avoids the mechanical singularity of the wrist during machining: the length of the scarfing tool is such to guarantee a certain inclination of the articulated arm with respect to the surface to machine; of course, this limitation has to be considered in the control system design. The horizontal configuration of the arm has to be maintained only during Rapid Motion, and unlocked preliminarily to any machining phase.

7.2. Scarfing kinematics and simulation

In order to show the functional compliance of the proposed architecture with the machining requirements, a kinematic simulation has been realized for a simple flat circular scarfing operation, reported in "Video 1", annexed to this paper. As stated in Section 2, the circular scarfing is a simplified case and, for this reason, the kinematic simulation will be clearer. The clip shows the mobile robot machining a scarfing pocket inside an aeronautical component. As simplification, only two CFRP ply layers are machined, with respectively diameters of 100 mm (the upper one, highlighted in red in the clip) and 80 mm (in blue), and 1 mm in depth, within a timeframe corresponding to 10 seconds for the largest first ply and proportional for the smaller one. The only aim of using this set of values is to analyze joint behaviors during a generic machining task; in a real scenario, adjacent plies to be removed would be much more similar in terms of diameters, the gap in depth direction smaller (about 0.1 mm) and the machining time to remove each ply much longer (in the order of some minutes). The Fig. 14 shows the tool position, the robot joints rotations and positions during the simulated scarfing operation of the two circular pockets on the first two layers. Tool trajectories on the flat surface of the component are showed as interpolated points on the top left of the figure. The green dashed line highlights the change along $\hat{x}$: layer 1 (toolpath on the left) is machined within the time interval $0 \div 10$ seconds; layer 2 (toolpath on the right) within $10 \div 18$ seconds. The pockets are machined with concentric circular paths (red arrows) with decreasing diameters (from outside towards inside). Discontinuities are evident in figures due to the transition between circular paths (highlighted with red circles in $p_{e,y}$ graph). The graph of $p_{e,x}$ shows the depth increment Δx at time $t = 10$ seconds to pass from first to second layer. The graphs of rod positions in c) show that the lateral rods follow the tool movement and push against the component walls, assuring the necessary stability during the scarfing.

In the simulated machining task, the longitudinal position of the tool $p_{e,z}$ is directly dependent on the parameter d_1 while ϑ_2, ϑ_3 and ϑ_4 concur to the determination of its transversal position and ϑ_5 is kept constant, as the spherical milling tool requires a certain orientation during machining. The quote variation along $\hat{x}_1$ corresponds to the gap between the plies in the simplified model. Regarding Rover kinematics, the position of damage is such that a longitudinal motion parallel with the reference side wall is allowed; according to this, α is kept constant, and consequently also rod orientations β_2 and β_3. On the other hand, β_1 and β_4 change in compliance with the other side wall, in order to ensure robot stability during motion, as shown in Fig. 14.

7.3. Some considerations about the stiffness of the robot

In robotic machining, quality is crucially affected by the stiffness of the robot, that depends on its actuators, structure, architecture and can be different in each configuration. Due to this, stiffness analyses are performed to take this property into account, and compensate the resulting error in tool positioning with an appropriate control strategy. On the practical side, an overall "stiffness matrix" K is obtained, representing the relation between static forces or torques applied and the consequent displacements or rotations; one example of such a procedure is reported in [43]. Different approaches, widely described in [44], are used for stiffness modeling. Among these, the "modified" Virtual Joint Method (VJM) consists in representing a kinematic chain as a series of a) rigid links, b) virtual joints, that are localized springs in which the elastic deformation of the links are lumped, and c) actuating

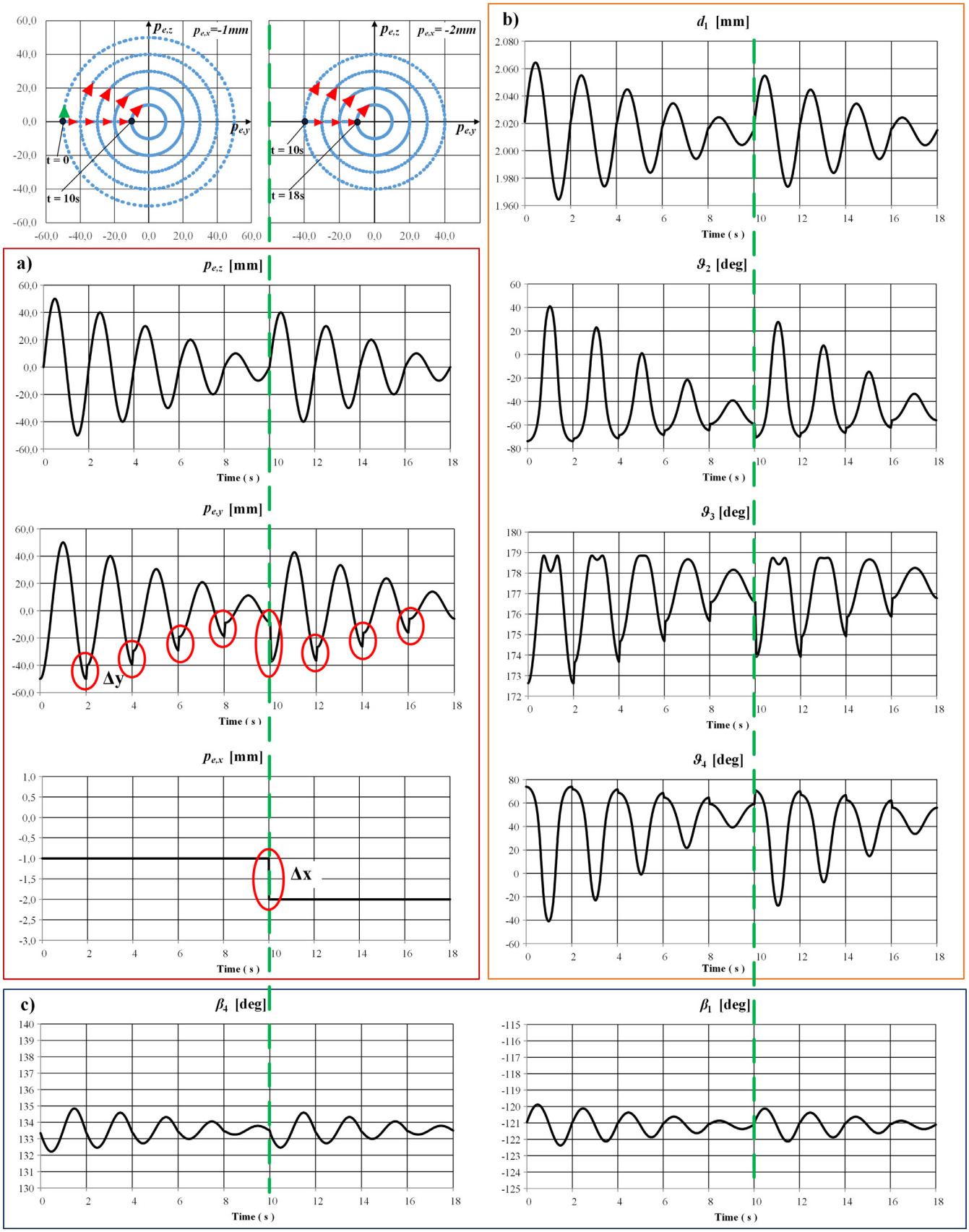

Fig. 14. Joint rotations and positions during the simulated machining: a) tool position (Top left); b) D-H parameters, ϑ5 = 0 constant (Top right); c) lateral rods position (Bottom).

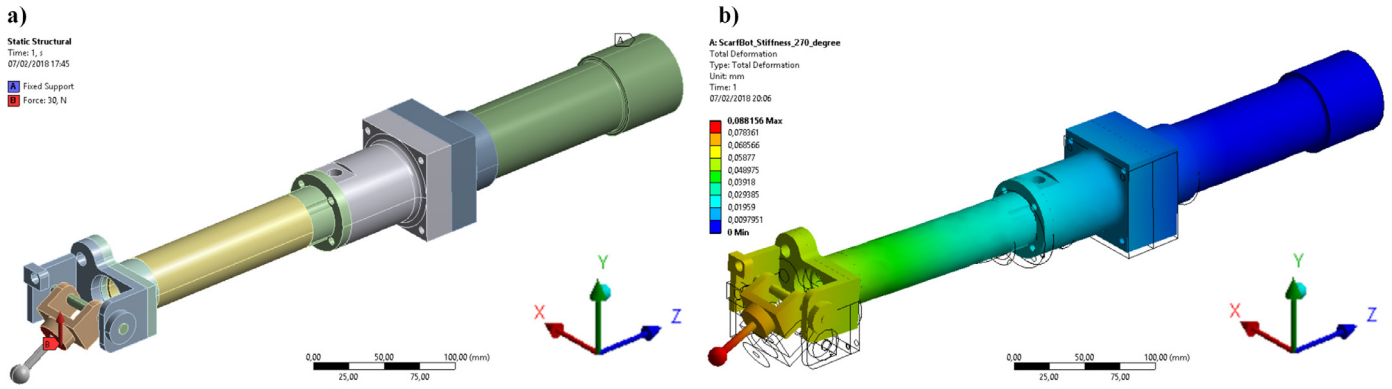

Fig. 15. FEM results: stiffness estimation of the arm link. Left: Main scarfing configuration and boundary conditions. Right: Amplified (Factor 350) total deformation of the arm overlapped to the initial geometry (wireframe).

joints that include virtual springs to model the stiffness of their mechanical transmissions and control loops [45]. In this approach, the stiffness each link is obtained by means of Finite Element Analyses FEA, performed considering the link origin fixed to the global coordinate system. On the other hand, the stiffness of the actuators is mainly determined by the mechanical transmissions, that can include a variety of components, leading to complicated structures or mechanisms. Due to this, the parameters related to actuators and joints are usually determined by means of static load experiments.

In the presented concept design, the Arm is characterized by a relevant length; the overall compliance is expected to be unneglectable, and a stiffness model will be required to apply the necessary compensations. Considering a subsequent parameter identification phase, a preliminary FEA analysis of the flexural behavior of the Arm is reported, in order to compute the end-effector deflection when the most critical load is applied. According to the "modified" VJM, the origin of the Arm is considered fixed. A 30 N force is applied on the tool, as normal component of the reaction of the machined surface in the worst load scenario. The analysis is performed with two different materials:

- Steel (Young's modulus E = 200 GPa, Poisson's ratio ν = 0.3), obtaining a displacement of the tool of 0.060 mm;
- T700 carbon-epoxy CFRP [46], with a displacement of 0.088 mm.

Fig. 15 shows the results of the FEA analyses. Although the obtained values are compliant with the accuracy required in the in-depth direction, it is expected that the practice will enable to obtain even better results, thanks to the definition of an appropriate stiffness model and the machining depth information, measured by the sensor on the tip of the robot and used as feedback in the control loop.

8. Conclusions

In the present work, the issue of repairing internal damages or manufacturing defects affecting a specific group of aeronautical components is addressed. The topic is particularly relevant, due to the lack of existing solutions: manual scarfing and application of repair plies, indeed, cannot be performed in the majority of the cases, due to the inaccessibility of the defected zone. A semi-autonomous scarfing mobile system concept is proposed, and its feasibility is demonstrated.

A mobile robotic system aimed to such machining operations must be capable of the required performance complying with the challenging geometrical and technological constraints. Due to this, several existing robotic solutions for demanding applications in confined spaces have been analyzed, and the most suitable strategies (i.e. the implementation of pushers for spatial stability inside tunnels) are taken into account. With these hypotheses, starting with the definition of all system requirements and aiming to an optimized solution, the present study is based on a task-oriented approach.

The proposed concept is composed by a multi-purpose mobile modular architecture (Rover and Semi-trailer), two interchangeable tools (Scarfing and Cleaning Forearms), and an articulated interface to equip them with the necessary mobility (Arm). The rover module is ready to host a specifically designed structured-light 3D scanner and a "Ply Application Forearm" would complete the robotic set to perform all the on-site operations. A control strategy is proposed to match two main requirements: 1) automatize some stages of the repair process (3D geometry reconstruction, positioning, toolpath calculation, scarfing, solvent deposition, etc.); 2) allow expert operators to supervise and monitor the operation and meet the required quality of the repair. In the Discussion section, some critical aspects are deepened, validating the concept design: compliance of the architecture with the requirements, machining functionalities and design of the Arm.

This study represents a step towards the automated repairing of internal inaccessible zones of aircraft components, proposing a novel solution based on a mobile robotic system.

Acknowledgments

This research was funded by the Italian Government and European Commission through the DITECO PON03PE_00067_2 Research Project aimed to develop repair technologies for large composite structures in aeronautics. The project was executed under the guide and partnership of the international aircraft manufacturer Leonardo S.p.A.

Supplementary materials

Supplementary material associated with this article can be found, in the online version, at doi:10.1016/j.rcim.2018.07.011.

Appendix A. Idef0 representation of Inspection, Scarfing and Cleaning tasks

The pictures A.1, A.2 and A.3 illustrate Scarfing and Cleaning Tasks according to Idef0 Standard.

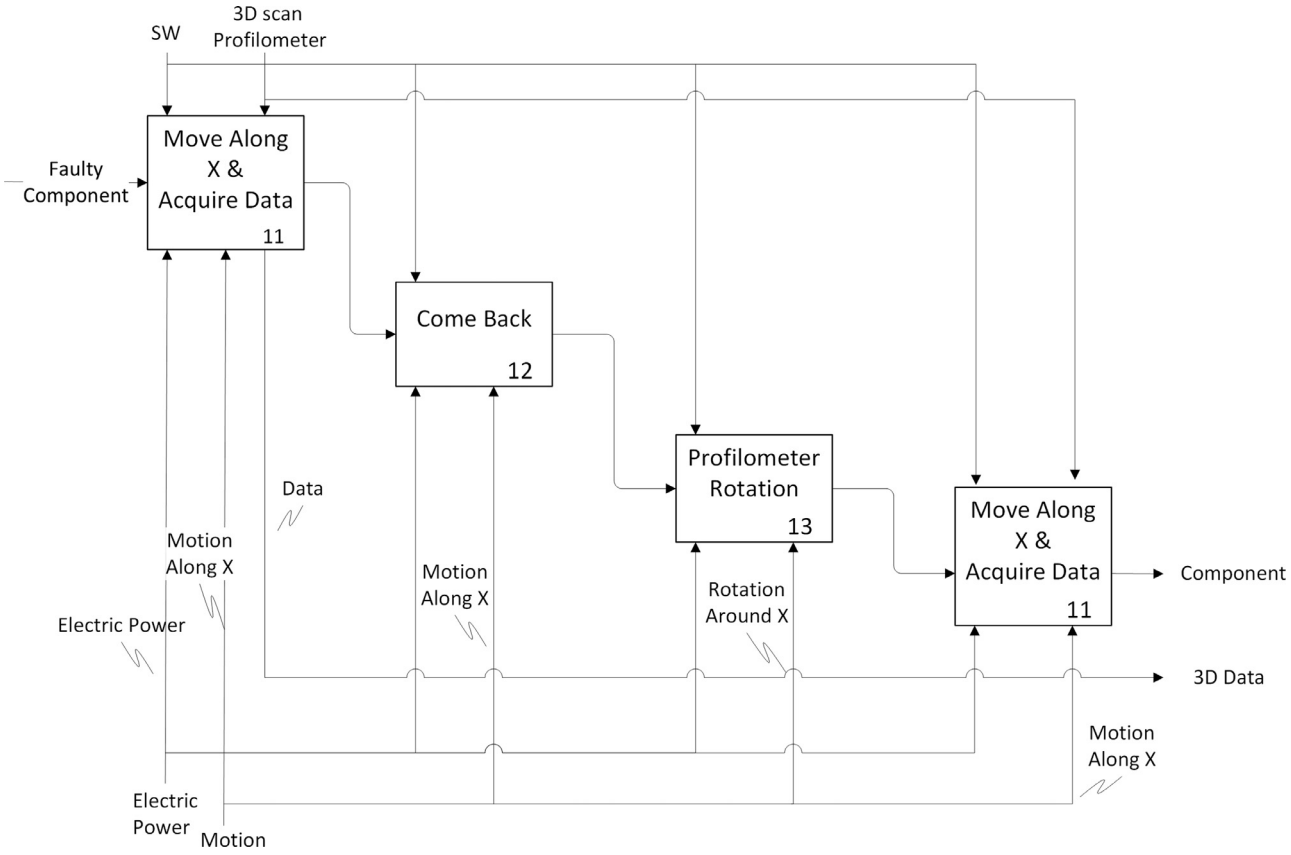

Fig. A.1. Representation, according to Idef0 standard, of the Inspection Tasks.

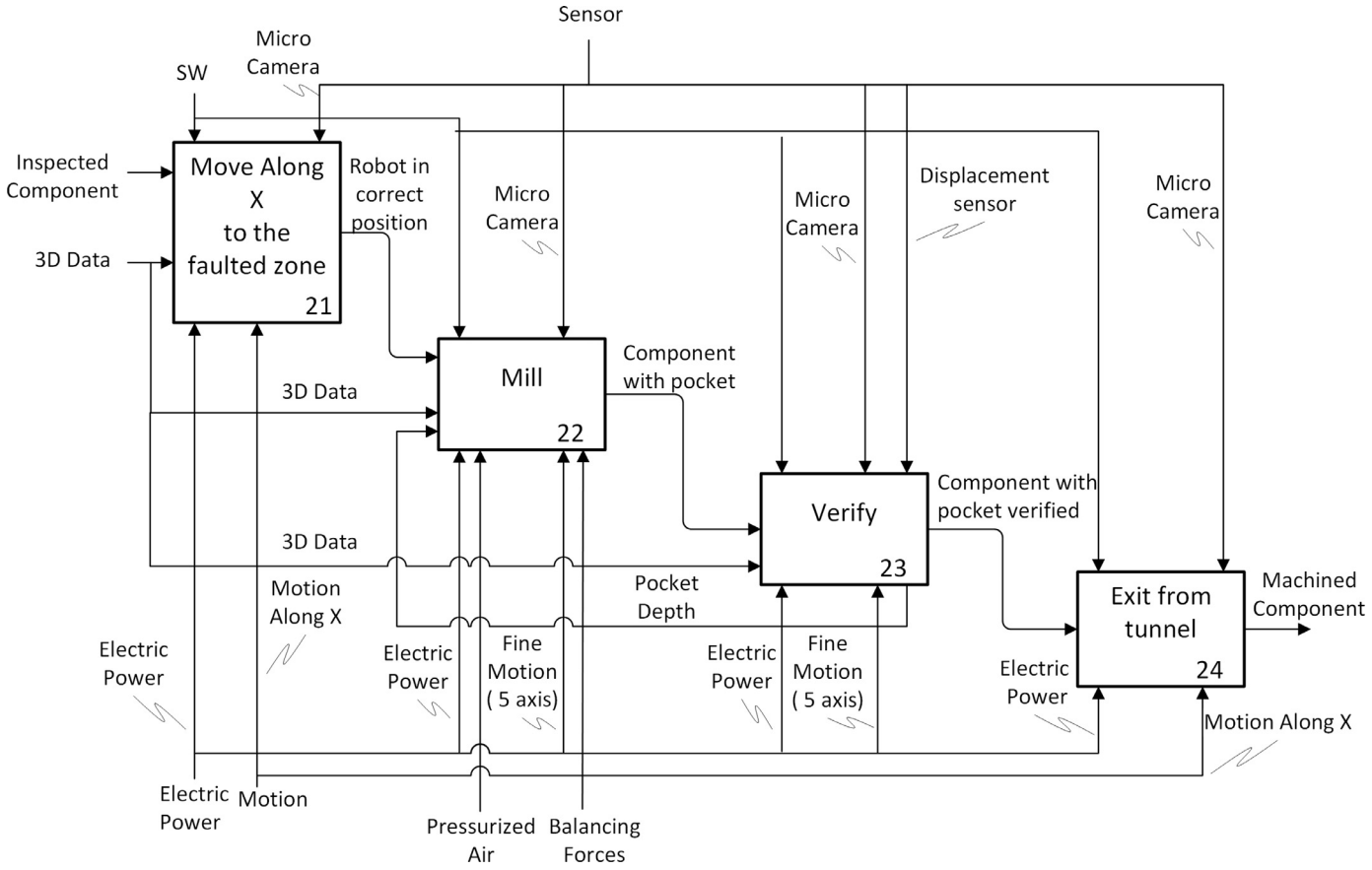

Fig. A.2. Representation, according to Idef0 standard, of the Scarfing Task.

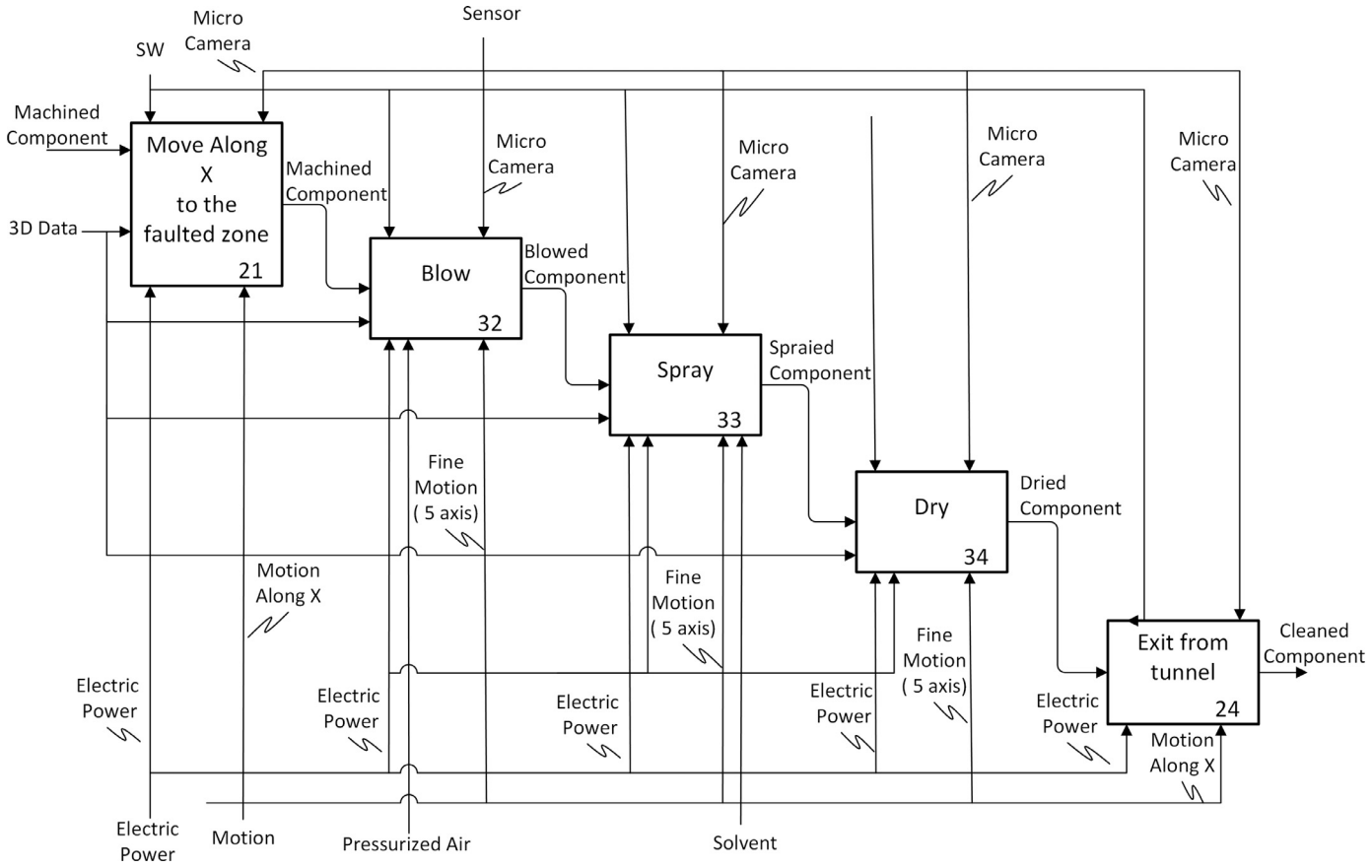

Fig. A.3. Representation, according to Idef0 standard, of the Cleaning Task.

Appendix B. Kinematic details

B.1. Rover Geometric Parameters

This section reports the main geometrical parameters for the Rover.

B.2. A_{05} Matrix composition

This section expands matrix $\mathbf{A}_{05}$, called in Section 3. Vectors $\hat{\mathbf{x}}_5$, $\hat{\mathbf{y}}_5$, $\hat{\mathbf{z}}_5$ and $\mathbf{p}_e$ are described separately in the following Equations:

$$\hat{\mathbf{x}}_5 = \begin{bmatrix} \cos(\vartheta_5)\cdot[\sin(\vartheta_2)\cdot\sin(\vartheta_4) + \cos(\vartheta_2)\cdot\cos(\vartheta_3)\cdot\cos(\vartheta_4)] + \cos(\vartheta_2)\cdot\sin(\vartheta_3)\cdot\sin(\vartheta_5) \\ \sin(\vartheta_2)\cdot\sin(\vartheta_3)\cdot\sin(\vartheta_5) - \cos(\vartheta_5)\cdot[\cos(\vartheta_2)\cdot\sin(\vartheta_4) - \cos(\vartheta_3)\cdot\cos(\vartheta_4)\cdot\sin(\vartheta_2)] \\ \cos(\vartheta_4)\cdot\cos(\vartheta_5)\cdot\sin(\vartheta_3) - \cos(\vartheta_3)\cdot\sin(\vartheta_5) \end{bmatrix} \tag{B.1}$$

Table B.1
Geometric parameters of the Rover.

Label	Description	Value [mm]
l_{wb}	Rover wheelbase	424
l_g	Rover Gauge	130
l_{lon}	Longitudinal distance between hinge axes of the pushers	168
l_{tra}	Transversal distance between hinge axes of the pushers	86
l_{str}	Length of the semitrailer	525
l_b	Length of each pusher	200
r_b	Radius of pusher rollers	20
l_D	Diagonal length (Rover + Semitrailer)	1024
d_2	Distance between the front traction unit axis from the extremity of the Rover	67
d_{msr}	Longitudinal distance of the robot from a reference panel, measured by the laser sensor	Variable
d_1	Distance between the root of the aeronautical component and the external reference panel	Variable

$$\hat{\mathbf{y}}_5 = \begin{bmatrix} \cos(\vartheta_2)\cdot\cos(\vartheta_5)\cdot\sin(\vartheta_3) - \sin(\vartheta_5)\cdot[\sin(\vartheta_2)\cdot\sin(\vartheta_4) + \cos(\vartheta_2)\cdot\cos(\vartheta_3)\cdot\cos(\vartheta_4)] \\ \sin(\vartheta_5)\cdot[\cos(\vartheta_2)\cdot\sin(\vartheta_4) - \cos(\vartheta_3)\cdot\cos(\vartheta_4)\cdot\sin(\vartheta_2)] + \cos(\vartheta_5)\cdot\sin(\vartheta_2)\cdot\sin(\vartheta_3) \\ -\cos(\vartheta_3)\cdot\cos(\vartheta_5) - \cos(\vartheta_4)\cdot\sin(\vartheta_3)\cdot\sin(\vartheta_5) \end{bmatrix} \tag{B.2}$$

$$\hat{\mathbf{z}}_5 = \begin{bmatrix} \cos(\vartheta_2)\cdot\cos(\vartheta_3)\cdot\sin(\vartheta_4) - \cos(\vartheta_4)\cdot\sin(\vartheta_2) \\ \cos(\vartheta_2)\cdot\cos(\vartheta_4) + \cos(\vartheta_3)\cdot\sin(\vartheta_2)\cdot\sin(\vartheta_4) \\ \sin(\vartheta_3)\cdot\sin(\vartheta_4) \end{bmatrix} \tag{B.3}$$

$$\mathbf{p}_e = \begin{bmatrix} d_4\cdot\cos(\vartheta_2)\cdot\sin(\vartheta_3) + a_5[\cos(\vartheta_5)\cdot(\sin(\vartheta_2)\cdot\sin(\vartheta_4) + \cos(\vartheta_2)\cdot\cos(\vartheta_3)\cdot\cos(\vartheta_4)) + \cos(\vartheta_2)\cdot\sin(\vartheta_3)\cdot\sin(\vartheta_5)] \\ d_4\cdot\sin(\vartheta_2)\cdot\sin(\vartheta_3) + a_5[\sin(\vartheta_2)\cdot\sin(\vartheta_3)\cdot\sin(\vartheta_5) - \cos(\vartheta_5)\cdot(\cos(\vartheta_2)\cdot\sin(\vartheta_4) - \cos(\vartheta_3)\cdot\cos(\vartheta_4)\cdot\sin(\vartheta_2))] \\ d_1 + d_2 - d_4\cdot\cos(\vartheta_3) + a_5[\cos(\vartheta_4)\cdot\cos(\vartheta_5)\cdot\sin(\vartheta_3) - \cos(\vartheta_3)\cdot\sin(\vartheta_5)] \end{bmatrix} \tag{B.4}$$

B.3. Solution of the Arm inverse kinematic problem

The problem is solved analyzing separately position and orientation. With reference to [42], the vector $\mathbf{p}_w$ can be expressed in both the ways reported in the following Equations:

$$\mathbf{p}_w = \mathbf{p}_e - a_5\cdot\hat{\mathbf{x}}_5 = \begin{bmatrix} p_{e,x} - a_5\cdot\cos(\theta)\cdot\cos(\varphi) \\ -a_5\cdot\cos(\theta)\cdot\sin(\varphi) \\ a_5\cdot\sin(\theta) \end{bmatrix} \tag{B.5}$$

$$\mathbf{p}_w = \begin{bmatrix} d_4\cdot\cos(\vartheta_2)\cdot\sin(\vartheta_3) \\ d_4\cdot\sin(\vartheta_2)\cdot\sin(\vartheta_3) \\ d_1 + d_2 - d_4\cdot\cos(\vartheta_3) \end{bmatrix} \tag{B.6}$$

The elements of the vector Equation B.5 are supposed known, as well as the operational variables $\mathbf{p}_{\text{Arm}}$ represent the input of the inverse kinematic problem. On the other hand, target of the inverse kinematics is to obtain joint variables $\mathbf{q}_{\text{Arm}} = [d_1\ \vartheta_2\ \vartheta_3\ \vartheta_4\ \vartheta_5]^{\text{T}}$. By comparing B.5 and B.6, the expressions for variables d_1, ϑ_2, ϑ_3 are obtained:

$$\vartheta_3 = \arcsin\left(\frac{\sqrt{p_{w,x}^2 + p_{w,y}^2}}{d_4}\right) \tag{B.7}$$

$$\vartheta_2 = \arcsin\left(\frac{p_{w,y}}{\sqrt{p_{w,x}^2 + p_{w,y}^2}}\right) \tag{B.8}$$

$$d_1 = p_{w,z} - d_2 - d_4\cdot\cos(\vartheta_3) \tag{B.9}$$

In order to determine joint variables ϑ_4 and ϑ_5, Equation B.10 is used, in which the second member does not contain unknown variables, obtaining the expressions in B.11 and B.12.

$$\mathbf{R}_{35}(\vartheta_4, \vartheta_5) = \mathbf{R}_{03}^{\text{T}}\cdot\mathbf{R}_{\varphi,\theta} \tag{B.10}$$

$$\vartheta_4 = \arcsin\left(\frac{\cos(\varphi)\cdot\cos(\theta)\cdot\sin(\vartheta_2) - \cos(\theta)\cdot\cos(\vartheta_2)\cdot\sin(\varphi)}{\cos(\vartheta_5)}\right) \tag{B.11}$$

$$\vartheta_5 = \arcsin(\cos(\vartheta_3)\cdot\sin(\theta) + \cos(\varphi)\cdot\cos(\theta)\cdot\cos(\vartheta_2)\cdot\sin(\vartheta_3) + \cos(\theta)\cdot\sin(\varphi)\cdot\sin(\vartheta_2)\cdot\sin(\vartheta_3)) \tag{B.12}$$

References

[1] K.B. Katnam, L.F.M. Da Silva, T.M. Young, Bonded repair of composite aircraft structures: a review of scientific challenges and opportunities, Prog. Aerosp. Sci. 61 (2013) 26–42 http://dx.doi.org/10.1016/j.paerosci.2013.03.003.

[2] K. Wood, In-situ composite repair builds on basics, High performance composites 2008 November.

[3] K.B. Armstrong, W. Cole, G. Bevan, Care and Repair of Advanced Composites, SAE International, London, 2005.

[4] J. Holtmannspötter, J.V. Czarnecki, F. Feucht, M. Wetzel, H.-J. Gudladt, T. Hofmann, J.C. Meyer, M. Niedernhuber, On the fabrication and automation of reliable bonded composite repairs, J. Adhes. 91 (1-2) (2015) Primary Bonded Repairs in Composite Structures.

[5] D. Holzhüter, A. Pototzky, C. Hühne, M. Sinapius, Automated *scarfing process for bonded composite re*pairs, Ch23 of, Adaptive, Tolerant and Efficient Composite Structures, Springer, 2012.

[6] E. Paquet, S. Garnier, M. Ritou, B. Furet, V. Desfontaines, Implementation of a new method for robotic repair operations on composite structures, in: B. Eynard, V. Nigrelli, S.M. Oliveri, G. Peris-Fajarnes, S. Rizzuti (Eds.), Advances on Mechanics, Design Engineering and Manufacturing, Springer, Catania, Italy, 2016, pp. 321–328, , https://doi.org/10.1007/978-3-319-45781-9_33.

[7] B. Mann, C. Reich, Automated repair of fiber composite structures based on 3D-Scanning and robotized milling, Deutscher Luft- und Raumfahrtkongress (2012) DocumentID: 281448.

[8] C. Mineo, C. MacLeod, M. Morozov, S.G. Pierce, R. Summan, T. Rodden, D. Kahani, J. Powell, P. McCubbin, C. McCubbin, G. Munro, S. Paton, D. Watson, Flexible Integration of Robotics, Ultrasonics and Metrology for the Inspection of Aerospace Components, AIP Conference Proceedings, 1806 (2016).

[9] GE Inspection Robotics, http://inspection-robotics.com/, 2016 (access 19/09/2016).

[10] NREC National Robotics Engineering Center, http://www.nrec.ri.cmu.edu/projects/explorer/, 2016 (access 19/09/2016).

[11] H. Schempf, E. Mutschler, V. Goltsberg, Gas Main Robotic Inspection System, U.S. Patent # 6,912,176 and international US2002190682 (A1). Applicants: Inventors, Carnegie Mellon University.

[12] H. Schempf, E. Mutschler, V. Goltsberg, G. Skoptsov, A. Gavaert, G. Vradis, 1st International Workshop on Advances in Service Robotics, ASER'03, Bardolino, Italy, 2003 March 13-15.

[13] Pure technology Ltd., https://www.puretechltd.com/technologies-brands/pure-robotics, (2016) (access 19/09/16).

[14] Redzone Robotics, 2016 (access 19/09/2016)visited on September 19th, http://www.redzone.com/products/solo-robots/, (2016).

[15] LLC. Envirosight, http://www.envirosight.com/rovverx_sat.php, (2016) (access 19/09/2016).

[16] Inuktun InCommand Robotics LLC., http://www.inuktun-europe.com/, (2016) (access 19/09/2016).

[17] Schroder sewer inspection camera, http://schroder.sell.everychina.com/, (2016) (access 19/09/2016).
[18] Robotics Design, http://roboticsdesign.qc.ca, (2016) (access 19/09/2016).
[19] Neovision, s. r. o., http://www.jettyrobot.com/, (2016) (access 19/09/2016).
[20] D. Lee, et al., "Development of a mobile robotic system for working in the double-hulled structure of a ship, J. Robot. Comput.-Integr. Manuf. 26.1 (2010) 13–23.
[21] Fraunhofer-Gesellschaft, Automated assembly of aircraft wings, Automatica Conf. 2014, Research news 30.04. 2014 https://www.fraunhofer.de/en/press/research-news/2014/may/automated-assembly-of-aircraft-wings.html, (2016) (access 19/09/2016).
[22] Xin Dong, et al., "Development of a slender continuum robotic system for on-wing inspection/repair of gas turbine engines, J. Robot. Comput.-Integr. Manuf. 44 (2017) 218–229.
[23] M. Agheli, Q. Long, S.N. Stephen, SHeRo: Scalable hexapod robot for maintenance, repair, and operations, J. Robot. Comput. Integr. Manuf. 30 (5) (2014) 478–488.
[24] C. Soutis, F.Z. Hu, Design and performance of bonded patch repairs of composite structures, Proc. Inst. Mech. Eng. Part G. J. Aerosp. Eng. 211 (4) (1997) 263–271.
[25] A.J. Gunnion, I. Herszberg, Parametric study of scarf joints in composite structures, Compos. Struct. 75 (1) (2006) 364–376.
[26] M.N. Charalambides, R. Hardouin, A.J. Kinloch, F.L. Matthews, Adhesively-bonded repairs to fiber composite materials I. Experimental, Compos. Part A Appl. Sci. Manuf. 29 (11) (1998) 1371–1381.
[27] A.A. Baker, L.R.F. Rose, R. Jones, first ed, Advances in the Bonded Composite Repair of Metallic Aircraft Structure 1 Elsevier Science, 2003.
[28] F. Fischer, L. Romoli, R. Kling, Laser-based repair of carbon fiber reinforced plastics, CIRP Ann. - Manuf. Tech 59 (2010) 203–206.
[29] D. Holzhüter, A. Pototzky, C. Hühne, M. Sinapius, Automated scarfing process for bonded composite repairs. Chapter 3.7. In: Wiedemann M., Sinapius M. (eds) Adaptive, Tolerant and Efficient Composite structures, 2013. Research Topics in Aerospace. Springer, Berlin, Heidelberg. doi:10.1007/978-3-642-29190-6_23.
[30] E. Paquet, A. Garnier, M. Ritou, B. Furet, V. Desfontaines, Implementation of a new method for robotic repair operation on composite structure, in: B. Eynard, V. Nigrelli, S. Oliveri, G. Peris-Fajarnes, S. Rizzuti (Eds.), Advances on Mechanics, Design Engineering and Manufacturing. Lecture Notes in Mechanical Engineering, Springer, Cham, 2017, , https://doi.org/10.1007/978-3-319-45781-9_33.
[31] C.H. Wang, C.N. Duong, Repair manufacturing processes, Chapter 9, Bonded Joints and Repairs to Composite Airframe Structures, (2016), pp. 243–264, https://doi.org/10.1016/B978-0-12-417153-4.00009-8.
[32] B. Whittingham, A.A. Baker, A. Harman, D. Bitton, Micrographic studies on adhesively bonded scarf repairs to thick composite aircraft structure, Compos. Part A Appl. Sci. Manuf. 40 (2009) 1419–1432.
[33] C.H. Wang, A.J. Gunnion, Optimum shapes of scarf repairs, J. Compos. Part A Appl. Sci. Manuf. 40 (9) (2009) 1407–1418, https://doi.org/10.1016/j.compositesa.2009.02.009.
[34] L.L. Mansberger, General Aviation Composite repair. Department of Mechanical and Aerospace Engineering, The University of Texas, Arlington, 2009.
[35] P.E. Irving, C. Soutis, Polymer Composites in the Aerospace Industry. Woodhead Publishing Series in Composites Science and Engineering. No. 50, 536 pages. Elsevier, 2015. ISBN Print: 978-0-85709-523-7; ISBN online: 978-0-85709-918-1.
[36] The Composite Materials Handbook (CMH-17), Volume 1: Guidelines for Characterization of Structural Materials. SAE International, 2012. Product Code: R-422, ISBN: 978-0-7680-7811-4, 719.
[37] The Composite Materials Handbook (CMH-17), Volume 3: Materials Usage, Design, and Analysis. SAE International, 2012. Product Code: R-424, ISBN: 978-0-7680-7813-8, 952.
[38] A. Baker, Development of a hard-patch approach for scarf repair of composite structure, Def. Sci. Technol. Organ. 19 (2006) Report TR1892.
[39] N.S. Hu, L.C. Zhang, A study on the grindability of multidirectional carbon fibre-reinforced plastics, J. Mater. Process. Tech. 140 (1-3) (2003) 152.
[40] R. Siegwart, I. Nourbakhsh, Locomotion, in: Introduction to Autonomous Mobile Robot, The MIT Press, Cambridge, Massachussetts, London, England, 2004, pp. 13–38.
[41] B. Siciliano, L. Sciavicco, L. Villani, G. Oriolo, Denavit–Hartenberg convention, in Robotics: modelling, Planning and Control, Springer, 2010, pp. 61–65.
[42] B. Siciliano, L. Sciavicco, L. Villani, G. Oriolo, Inverse kinematics problem, Robotics: Modelling, Planning and Control, Springer, 2010, pp. 90–100.
[43] C. Dumas, S. Caro, C. Mehdi, S. Garnier, B. Furet, Joint stiffness identification of six-revolute industrial serial robots, J. Robot. Comput. Integr. Manuf. 27 (4) (2011) 881–888 Elsevier.
[44] A. Klimchik. Enhanced stiffness modeling of serial and parallel manipulators for robotic-based processing of high performance materials. Robotics [cs.RO]. Ecole Centrale de Nantes (ECN); Ecole des Mines de Nantes, 2011.
[45] A. Pashkevich, D. Chablat, P. Wenger, Stiffness Analysis of Overconstrained Parallel Manipulators, Mech. Mach. Theory 44 (5) (2009) 966–982 Elsevier.
[46] M. Nirbhay, A. Dixit, R.K. Misra, H. Singh Mali, Tensile Test simulation of CFRP test specimen using finite elements, Procedia Mater. Sci. 5 (2014) 267–273, https://doi.org/10.1016/j.mspro.2014.07.266.